



Calhoun: The NPS Institutional Archive
DSpace Repository

Theses and Dissertations

Thesis and Dissertation Collection

1976

Laser generated magnetic fields.

Williamson, Francis Thomas

<http://hdl.handle.net/10945/17833>

Downloaded from NPS Archive: Calhoun



Calhoun is a project of the Dudley Knox Library at NPS, furthering the precepts and goals of open government and government transparency. All information contained herein has been approved for release by the NPS Public Affairs Officer.

Dudley Knox Library / Naval Postgraduate School
411 Dyer Road / 1 University Circle
Monterey, California USA 93943

<http://www.nps.edu/library>

LASER GENERATED MAGNETIC FIELDS

Francis Thomas Williamson

NAVAL POSTGRADUATE SCHOOL

Monterey, California



THESIS

LASER GENERATED MAGNETIC FIELDS

by

Francis Thomas Williamson, Jr.

June 1976

Thesis Advisor: Fred R. Schwirzke

Approved for public release; distribution unlimited.

T174990

REPORT DOCUMENTATION PAGE		READ INSTRUCTIONS BEFORE COMPLETING FORM
1. REPORT NUMBER	2. GOVT ACCESSION NO.	3. RECIPIENT'S CATALOG NUMBER
4. TITLE (and Subtitle) LASER GENERATED MAGNETIC FIELDS		5. TYPE OF REPORT & PERIOD COVERED Master's Thesis; June 1976
7. AUTHOR(s) Francis T. Williamson, Jr.		6. PERFORMING ORG. REPORT NUMBER
9. PERFORMING ORGANIZATION NAME AND ADDRESS Naval Postgraduate School Monterey, California 93940		8. CONTRACT OR GRANT NUMBER(s)
11. CONTROLLING OFFICE NAME AND ADDRESS Naval Postgraduate School Monterey, California 93940		10. PROGRAM ELEMENT, PROJECT, TASK AREA & WORK UNIT NUMBERS
14. MONITORING AGENCY NAME & ADDRESS (if different from Controlling Office) Naval Postgraduate School Monterey, California 93940		12. REPORT DATE June 1976
		13. NUMBER OF PAGES 88
		15. SECURITY CLASS. (of this report) Unclassified
		15a. DECLASSIFICATION/DOWNGRADING SCHEDULE
16. DISTRIBUTION STATEMENT (of this Report) Approved for public release; distribution unlimited		
17. DISTRIBUTION STATEMENT (of the abstract entered in Block 20, if different from Report)		
18. SUPPLEMENTARY NOTES		
19. KEY WORDS (Continue on reverse side if necessary and identify by block number) Crater dependence of laser generated magnetic fields Laser crater cross-sections X-ray detection from laser plasma		
20. ABSTRACT (Continue on reverse side if necessary and identify by block number) A sequence of laser pulses focussed onto the same spot on a target produces evaporation of target material and the formation of a crater with crater depth increasing from shot to shot. An experimental study of the crater-depth dependence of the magnetic fields generated by the laser produced plasmas has been performed. Repeated irradiation of an Aluminum target with a laser pulse of 10^{12} W/cm ² in a low background pressure of air at 10^{-5} Torr		

produced magnetic fields as high as 1500 G and at a rate of .055 mm/shot excavated a hole nearly 4mm deep and 2mm wide at the target surface. Optical micrographs were taken of the target crater surface and of craters sectioned for examination by a Scanning Electron Microscope.

An independent determination of the plasma-electron temperature was obtained from the x-ray continuum of the plasma.

LASER GENERATED MAGNETIC FIELDS

by

Thomas
Francis T. Williamson, Jr.
Lieutenant Commander, United States Navy
B.S., University of Wisconsin, 1966

Submitted in partial fulfillment of the
requirements for the degree of

MASTER OF SCIENCE IN PHYSICS

from the

NAVAL POSTGRADUATE SCHOOL

June 1976

ABSTRACT

A sequence of laser pulses focussed onto the same spot on a target produces evaporation of target material and the formation of a crater with crater depth increasing from shot to shot. An experimental study of the crater-depth dependence of the magnetic fields generated by the laser produced plasmas has been performed .

Repeated irradiation of an aluminum target with a laser pulse of 10^{12} W/cm² in a low background pressure of air at 10^{-5} Torr produced magnetic fields as high as 1500 G and at a rate of .055 mm/shot excavated a hole nearly 4 mm deep and 2 mm wide at the target surface. Optical micrographs were taken of the target crater surface and of craters sectioned for examination by a Scanning Electron Microscope.

An independent determination of the plasma-electron temperature was obtained from the x-ray emission continuum of the plasma.

TABLE OF CONTENTS

I.	INTRODUCTION.....	11
II.	PREVIOUS EXPERIMENTAL WORK.....	13
III.	THEORY.....	15
	A. SELF-GENERATED MAGNETIC FIELDS.....	15
	B. INTERACTION WITH AMBIENT PLASMA.....	19
	C. PLASMA X-RAY EMISSION.....	21
IV.	EXPERIMENTAL ARRANGEMENT.....	25
	A. LASER.....	25
	B. LASER MONITORING TECHNIQUES.....	25
	C. VACUUM CHAMBER.....	26
	D. TEMPORAL REFERENCE.....	27
	E. PHOTODIODES.....	28
	F. MAGNETIC PROBE.....	29
	1. Construction.....	29
	2. Calibration.....	30
	3. Signal Integration.....	30
	4. Reliability.....	32
	G. EXPERIMENTAL METHODS.....	32
	H. DATA COLLECTION ERROR ESTIMATES.....	34
	1. Spatial.....	35
	2. Temporal.....	35
	3. Probe Perturbations.....	35
V.	DATA AND RESULTS.....	37
	A. OBSERVATIONS.....	37
	B. CHAMBER DIMENSIONS.....	38
	C. SELECTED DATA.....	41
	1. Probe Position (3,0,1.5).....	42
	2. Probe Position (4,0,1).....	43
	3. Probe Position (7,0,1).....	44
	D. DATA ANALYSIS.....	44

VI. SUMMARY.....	53
A. CONCLUSIONS.....	53
B. PROPOSALS FOR CONTINUED RESEARCH.....	54
LIST OF REFERENCES.....	83
LIST OF FIGURES.....	7
LIST OF TABLES.....	9
INITIAL DISTRIBUTION LIST.....	87

LIST OF FIGURES

1. Conceptual plasma representation and the orientation of the two x-ray photodiode detectors.....	56
2. Laser system arrangement and experimental set-up....	57
3. Vacuum chamber (top view).....	58
4. Magnetic probe construction.....	59
5. Calibration curves for magnetic probes..	60
6. Circuit diagram for the passive RC integrator and the magnetic probe.....	61
7. Cylindrical polar coordinate system orientation.....	62
8. Magnetic field time rate of change signals for shots 1,3,5 and 16.....	63
9. Magnetic field signals for shots 1,15 and 38 at probe position (4,0,1).....	64
10. Temporal sequence of laser, x-ray photodiode and magnetic field signals for probe position (4,0,1).....	65
11. Optical micrograph of entry hole in Al target for shots 1 and 11.....	66
12. Optical micrograph of entry hole for shot 40 and of the crater splash zone.....	67
13. Crater radius as a function of shot number.....	68
14. Scanning electron microscope photograph of a crater burned into an Al target after 8 and 30 shots.....	69
15. Scanning electron microscope photograph of a crater	

burned into an Al target after 61 and 65 shots.....	70
16. Graphical representation of crater and detail of crater dimensions.....	71
17. Measured electron temperature as function of irradiance on the target.....	72
18. Magnetic field strength as function of shot number for probe location (3,0,1.5).....	73
19. Magnetic field strength as function of shot number for probe location (4,320,1).....	74
20. Magnetic field strength as function of shot number for probe location (4,0,1).....	75
21. Magnetic field strength as function of shot number for probe location (7,0,1).....	76
22. Energy-normalized values of magnetic field generation in Gauss per Joule as function of shot number for probe position (3,0,1.5).....	77
23. Energy-normalized values of magnetic field generation in Gauss per Joule as function of shot number for probe position (4,320,1).....	78
24. Energy-normalized values of magnetic field generation in Gauss per Joule as function of shot number for probe position (4,0,1).....	79
25. Energy-normalized values of magnetic field generation in Gauss per Joule as function of shot number for probe position (7,0,1).....	80
26. Graphical representation of line of sight from probe positions to the center of the crater.....	81
27. Arrival time of B_{\max} as function of shot number.....	82

LIST OF TABLES

I. CRATER DIMENSIONS.....40
II. LINEAR REGRESSION RESULTS.....46

ACKNOWLEDGEMENT

I wish to acknowledge the valuable technical help of Eck Saunders whose rapid response and cooperative attitude made the experiment run smoothly.

Special thanks to Professor Schwirzke who suggested and guided this investigation and to Professor Cooper for his readiness to discuss ideas and problems.

To my wife, Georgia, and my children I wish to convey my deep appreciation and love for their patience and understanding.

I. INTRODUCTION

Since the discovery of spontaneously generated magnetic fields in laser produced plasmas by Korobkin and Serov [18] and by Stanger [33] this area of research has become the object of intensive theoretical and experimental studies. The interest is due to the possible significance of these fields in proposed laser-driven pellet implosion fusion schemes.

Computer simulations have indicated the presence of megagauss magnetic fields being generated near the focal spot of high power laser produced plasma. Fields of this magnitude can have a substantial affect on the transport properties of laser-fusion plasmas [37].

The possible importance of these magnetic fields created the need for the systematic surveying of the magnetic fields and particle density profiles, including pressure dependence, from the laser produced plasma conducted by McKee [19], Ercoks [6] and Bird [2]. During Bird's research he noted the presence of an early rapidly propagating magnetic signal which was later investigated by Ercoks. Ercoks' analysis indicates that the early plasma signal is composed of electrons and ions with arrival times ranging from 80-100 nsec depending on probe location. While mapping these plasma density profiles with a double probe Ercoks decided to burn a crater into the target and note any anomalous behavior from previous plasma profiles. After firing 50 shots and excavating a 1 cm deep hole into an aluminum alloy target Brooks reported little observed change in the plasma expansion. From this observation Ercoks

suggested that the expansion dynamics from the hole were independent of the manner in which the plasma reached the target surface from the crater.

Characteristically the main plasma expands rapidly in the radial direction to a diameter of approximately 2.4 cm. at which point its radial expansion ceases and the plasma plume expands symmetrically along the target normal. This behavior suggested the presence of a radial confining force acting on the expanding plasma. Drouet and Bolton [13] reveal an active participation of the target in the current flow process. The immediate response of the current to the laser pulse suggests that the source of the current-magnetic field is near the target-plasma interface.

This investigation was undertaken to study the possible dependence of the spontaneously generated magnetic fields on the target cratering and to determine if the cratering has any effect on the radial confining force that produces the noted plasma behavior.

This thesis is divided into six sections. Section II contains the previous experimental work concerning the self-generated magnetic fields. Section III presents the theory related to the study of these magnetic fields and their possible interactions with the target or the ambient background plasma. Section IV contains the experimental arrangement. Section V discusses the data and the results and Section VI gives a summary with conclusions and recommendations for further research.

II. PREVIOUS EXPERIMENTAL WORK

The discovery of self-generated magnetic fields in laser produced plasmas opened an entire new area for experimentation. In particular researchers have been attempting to analyze the mechanisms by which the initial laser energy contained in the beam was coupled into the target and the resultant streaming plasma. Wegener [35] provides the history of the experiments conducted which led to the detailed investigations of self-generated magnetic fields performed more recently at the Naval Postgraduate School.

McKee [19] undertook the task to determine the dependence of self-generated magnetic fields on position, time, incident laser power and ambient background pressure. Some of the salient features noted were the increase of the magnetic field strength when the background pressure was increased, the fields azimuthal symmetry around the target normal and the small reverse magnetic field which occurred after several hundred nanoseconds. McKee proposed a density shell model to explain plasma magnetic field behavior. The pressure dependence of self-generated magnetic fields was further investigated by Bird [2]. In addition to magnetic probes, electric double probes were used. Bird was not able to confirm the density shell model, no density shell being observed. The pressure dependence of the fields was thoroughly investigated and a new model, detailed in a later section, was used to explain plasma behavior. An early magnetic signal was observed by Bird and this early signal was investigated by Brooks [6] and Wegener [35]. On the basis of Ericks' work which included, in part, the burning

of a crater into an aluminum target with no apparent change in the streaming plasma expansion prompted the research by Callahan [7] on plasma plume particle velocities and this investigation of crater-depth dependence of the magnetic field.

III. THEORY

A. SELF-GENERATED MAGNETIC FIELDS

The possible presence of induced magnetic fields was first deduced by Basov [1] in 1966. While conducting experiments on plasma produced by a giant laser pulse on a solid target he noted that the decaying plasma emits electrons whose currents reach tens of amperes and that these currents should induce a magnetic field.

J.A. Stamper, K. Papadopoulos, R.N. Sudan, S.C. Dean, E.A. McLeer and J. Dawson [33] attributed the generation of the observed magnetic fields to thermoelectric currents. These currents were thought to be associated with a thermoelectric junction formed by the laser focus and the plasma.

Investigation of the probable source of these magnetic fields, large non-colinear temperature and density gradients, was limited by the interference of the detecting probe in the laser light-plasma interface. A more recent experiment by M.G. Irouet and R. Bolton [13] on the currents associated with these self-generated magnetic fields circumvented part of this inhibiting limitation. The current-flow, through the plasma-target interface, was monitored by a small probe imbedded in a specially designed target. The results revealed an active participation of the target in the current-flow process with the existence of anodic and cathodic regions.

The accepted model for production of the laser plasma requires absorption of the laser energy by the electron fluid. Assuming a two fluid model of electrons and ions in a collision dominated neutral plasma leads to the development of equations governing the production of spontaneous magnetic fields as detailed by Stamper [33] and Schwirzke [30]. Assuming that during the plasma heating phase by the laser the electron temperature is much greater than the ion temperature means the electrons respond to the Lorentz forces in a background of relatively unresponsive ions. The equation of motion for the electron fluid is given by:

$$(1) \quad \rho \frac{\partial \mathbf{v}_e}{\partial t} = -en_e (\mathbf{E} + \mathbf{v}_e \times \mathbf{B}) - \nabla P_e + (en_e / \sigma) \mathbf{j}$$

where ρ is the electron mass density, \mathbf{v}_e the fluid velocity of electrons, P_e the pressure \mathbf{j} the current density, and σ the electrical conductivity. A scalar electron pressure is assumed since the velocity distribution within the volume of consideration is isotropic based on the electron-electron collision time which is much smaller than the pulse duration. If the electron inertia term is considered insignificant, equation (1) can be set equal to zero and solved for \mathbf{E} which yields:

$$(2) \quad \mathbf{E} = (\mathbf{j} / \sigma) - (\mathbf{v}_e \times \mathbf{B}) - (1 / en_e) \nabla P_e$$

The magnetic field equation can be obtained by taking the curl of equation (2) and combining this result with Maxwell's equations. Equation (2) becomes,

$$(3) \quad \partial B / \partial t = - (1/\sigma) (\nabla \times j) + \nabla \times (\mathbf{v} \times B) + \nabla \times (1/en_e) \nabla P_e$$

The term $\nabla \times j$ can be manipulated by applying $\mu_0 j = \nabla \times B$ and $\nabla \cdot B = 0$,

$$(4) \quad (1/\sigma) \nabla \times j = (1/\mu_0 \sigma) \nabla^2 B$$

which constitutes a diffusion term.

The second term describes the convective transport of the magnetic field. The ratio of the convective term and the diffusion term is the magnetic Reynolds number. When it is greater than 1 the flow term dominates and the magnetic field lines are to some extent frozen in the moving plasma. If it is less than 1 the diffusion term is more influential and the field energy is converted to internal energy through Joule heating. This means that the magnetic field is less affected by the plasma motion. The diffusion time is the decay time of the magnetic field given by $t = \mu_0 \sigma L^2$ where L is the average characteristic length of the flow and is related to the Reynolds number by,

$$(5) \quad R_m = \mu_0 \sigma L V$$

The third term $\nabla \times (1/en_e) \nabla P_e$ is the source term responsible for the generation of the spontaneous magnetic fields. Assuming an equation of state $P_e = n k T_e$ this term

yields:

$$(6) \quad \nabla \times \left(\frac{1}{en_e} \right) \nabla P_e = \nabla \times \left(\frac{k}{e} \nabla T_e + \left(\frac{kT_e}{en_e} \right) \nabla n_e \right)$$

Application of the vector identity $\nabla \times (a\mathbf{B}) = \nabla a \times \mathbf{B} + a(\nabla \times \mathbf{B})$ equation (6) simplifies it to,

$$(7) \quad \mathbf{S} = \left(\frac{k}{e} \right) \nabla T_e \times \left(\frac{1}{n_e} \right) \nabla n_e$$

\mathbf{S} denoting the source term. Clearly, this shows that magnetic field generation results from non-colinear temperature and density gradients.

The radial temperature gradient and the density gradient in the Z-direction may be approximated to provide an order of magnitude estimate of the magnetic induction near the focal spot [30]

$$(8) \quad B \leq \frac{k}{e} \left(\frac{T_e}{r_0} \nabla_i \right)$$

where r_0 is the focal spot radius and ∇_i is the ion expansion velocity in the axial direction.

A plasma created by a cylindrically symmetric laser beam from a planar target is axisymmetric about its expansion direction. Figure 1 depicts the geometry of this plasma. Density and temperature gradients can be found in both the radial and normal directions. The largest temperature gradient will be in the radial direction due to the laser heating of the plasma. The largest density gradient will be along the target normal produced from the plasma expansion in that direction. This combination of temperature and density gradients produce azimuthal magnetic fields.

Stamper and Tidman [34] have shown that electromagnetic field energy can be converted directly to magnetic field energy by radiation pressure. Radiation pressure is defined as the time average of the momentum flow tensor for the electromagnetic field. Radiation pressure produces a solenoidal electric field and must be included in equation (6) and therefore the source term equation (7). This radiation pressure results in a non-thermal source for the magnetic fields which have been found to be important at intensities above 10^{14} W/cm² for plasmas produced by a neodymium-doped glass laser. This intensity is several orders of magnitude above those used in this investigation and therefore is not included in any analysis considered.

B. INTERACTION WITH AMBIENT PLASMA

Absorption of the laser radiation by the target results in the vaporization of material from its surface. This vaporized material then continues to absorb laser radiation, and a hot, dense, ionized plasma results. This laser-produced plasma now expands in the axial and radial directions in an effort to achieve its lowest potential energy. As the plasma streams out it begins to couple with any ambient plasma present and energy is exchanged.

Photoionization of the initially neutral background gas by intense uv emission from the high-density laser plasma is a mechanism which can alter the ambient medium into which the plasma expands, so that plasma-plasma, as well as plasma-neutral, interactions can occur between the counterstreaming media.

During his investigations of self-generated magnetic

fields McKee [19] used a model developed by Dean, McLean, Stamper and Griem [15] to explain the interaction between a laser plasma and an ambient background plasma. Dean noted an expanding luminous interaction front which had well defined boundaries. The distance to which the front expanded was found to be a function of the pressure of the ambient background gas. The dependence of the expansion velocity on the background pressure was taken to be an indication of the coupling of the two plasmas. The dynamics of the laser plasma were found to be in agreement with a strong momentum-coupling model, and a collisionless interaction model was proposed. One possible mechanism is the ion-ion two stream instability in the presence of a magnetic field. The interaction front was thought of as a shell with increased density because the background ions are swept up by the luminous front and reach approximately the velocity of the front.

Wright [38] challenged the collisionless model for interactions between interstreaming ions. It was shown that the results of the experiments conducted by Dean, McLean, Stamper and Griem could be explained by collisional processes. The existence of the enhanced density shell was not challenged.

Bird [2] found no evidence of the density shell in his investigation. To explain the interaction and the field reversal Bird used the model proposed by Koppman [17] This model of multi-Coulomb collisions between the two plasmas assumes that the law of conservation of momentum could be applied to compute the velocity of the combined laser and background plasma from their initial spatial and velocity distributions. A shell-like interaction region was assumed to contain the photoionized plasma mass swept up by the shell and a fraction of the laser-produced plasma as it expands from the origin.

An interaction front has been detected and studied. It decelerates with a dependence on the background density. This deceleration seemed time dependent in a manner consistent with a momentum coupling between the laser plasma and the ambient plasma. Thus the ionized fraction of the background plasma was swept up by the leading edge of the expanding laser plasma. Increased mass in the streaming plasma means that the expansion velocity must decrease if the law of conservation of momentum is to hold.

Bird's model assumes that a large portion of the kinetic energy of the ambient plasma ions is converted to thermal energy. This occurs when the ambient plasma ions are captured within the interaction region. The possible mechanism for the heating is ion viscous forces. Due to the deceleration or pile-up of the laser plasma behind the interaction region there will be strong viscous heating there also.

Bird also assumed that the ambient plasma electrons undergo compressional heating in the interaction region during the early stages of the plasma expansion. The heating which causes the production of the large axial ion temperature gradient is assumed to be transmitted to the electrons by electron-ion collisions.

C. PLASMA X-RAY EMISSION

The energy absorbed by the target is partitioned in a variety of forms, i.e., magnetic field, fluid potential and kinetic, ion and electron thermal, ion internal and radiation field energies. Approximately 15% of the incident energy is emitted from the plasma in the form of continuum radiation and the characteristic spectral lines of the target

particles highly ionized states. Most of this radiant energy has short wavelength, less than 100 Angstroms, placing it in the soft x-ray range [29]. Soft x-rays with low penetrative power fall into the energy band of about 100eV to about 10keV.

The continuum portion of the x-ray emission may be used for determination of plasma electron temperatures and anomalous heating effects. The dependence of high-energy x-ray emission cut-off on temperature allows determination of the high-energy continuum wavelength distribution and therefore a sensitive measurement of the plasma electron temperature [15]. Extensive research and detail of plasma x-ray emission processes is contained in the introduction and theory of Shewchuk's [31] thesis which presents the first efforts of the Naval Postgraduate School to determine the plasma electron temperature of a laser produced plasma from x-ray emission.

The method employed in this research was to measure the relative transmission through two Beryllium absorption filters of different thickness. Absolute intensities of continuum radiation depend directly on plasma densities, however the spectral distribution depends on temperature in an exponential form as in equation (9),

$$(9) \quad I(E) = I_0 \exp \{-E/kT_e\}$$

where E is the x-ray photon energy [4]. The intensity drops off sharply whenever the condition $E \gg kT_e$ is met. For an electron temperature of 100 eV and x-rays in the range of 1 keV the intensity is reduced to $4.5 \times 10^{-5} I_0$.

The relative intensity method utilizes this x-ray exponential distribution by placing an absorption filter in front of the x-ray continuum detector. From end measurements with these absorption filters the electron temperature is determined from the slope of the x-ray continuum, when no spectral lines are present in the wavelength region and an exponential decay of the continuum is expected.

Experimental ratios obtained by this rather simple comparison technique are applied to curves determined from extensive numerically solved computer plots for a range of foil thicknesses, various foil materials and several electron temperatures [16,22,23]. Shewchuk [31] in his developmental research on x-ray detection has developed graphs from these computer solutions for the absorption filters (foils) used at Naval Postgraduate School. Utilizing these graphs, and observing the precautions for their application a reasonable electron temperature may be obtained.

This electron temperature may change in time and only apply to a fraction of the plasma being studied if the distribution of the particles is non-Maxwellian [26]. Since the size of the plasma produced in this study was no larger than several millimeters the value obtained was considered representative of the entire plasma.

The validity of using the electron temperature to represent the plasma temperature and the entire plasma can be seen by considering the equilibration time for transfer of absorbed energy from electrons to ions [27].

$$(10) \quad t_e = 252 AT^{3/2} / n_e z^2 \ln \Lambda$$

where $\ln \Lambda$ (the Coulomb logarithm) is a function which, for wide ranges of plasma parameters, is of the order of magnitude of 10, A is the atomic weight of the ions, the electron density n_e is in cm^{-3} , z is the ionic charge and T is the plasma temperature in degrees Kelvin. For an aluminum plasma ($A=27, Z=3$) with an electron temperature of 1.16×10^6 K, or equivalently 100eV, and a density of 10^{21} cm^{-3} , equilibration time is

$$t_e = 9.4 \times 10^{-11} \text{ sec}$$

which is smaller than the scale time of the Nd laser pulse $t_p = 25$ nsec. Since $t_p \ll t_e$ the electrons can effectively transfer absorbed energy to the ions during the pulses justifying both previous assumptions.

IV. EXPERIMENTAL ARRANGEMENT

A. LASER

The laser used in this investigation was a Korad K-1500 Q-switched neodymium-doped glass laser system. The system consists of an oscillator laser (K-1) which generates the initial 25 nsec (full width at half power) pulse through Q-switching by a Pockels cell. The output beam is then expanded by the expansion optics from the 1.27 cm diameter of the oscillator rod to the 1.94 cm diameter of the laser amplifier rod. The amplifier (K-2) amplifies the energy of the pulse. The arrangement of the laser system components is shown in Figure 2. The output of the laser system can be controlled by variation of the voltage applied to the flashlamps of the Nd oscillator and in the laser amplifier. The range of obtainable energies is 3.5 to 13 Joules. The duration of the laser pulse is 25 nsec which gives a range of output powers from 140 to 520 MW. The laser focal spot size radius is approximately .15 mm which gives a power density of $3.96 \times 10^{11} \text{ W/cm}^2$ for the energy of 7 Joules.

A more detailed description of the laser system is given in Davis' Thesis [11].

B. LASER MONITORING TECHNIQUES

In order to diagnose the laser beam a Korad K-D1 photodiode was used. Approximately 4% of the beam is reflected by a glass slide used as a beam splitter to a MgO diffusor block. The reflection from the block is monitored by the K-I1 photodiode after passing through a 0.1% neutral density filter. The photodiode provides two signals, one proportional to the pulse power, the other proportional to the laser pulse energy. The photodiode energy signal was calibrated using a Korad K-J3 Laser Calorimeter. The calorimeter was used to provide an absolute measure of the incident laser pulse energy against which the voltage reading on the Tektronix 564 b storage oscilloscope, which was used to display the energy signal, could be calibrated.

The power output signal was used to trigger a Tektronix 7904 oscilloscope. The energy output was monitored on every shot. The pulse width which was more reliable was checked before and after each series of measurements.

C. VACUUM CHAMBER

The target used was a .63 cm thick disk of aluminum alloy plate. The target diameter was 5.08 cm and the target could be rotated as desired.

The target was located in a vacuum chamber as shown by Figure 3. The chamber allows diagnosis of the laser produced plasma by optical means or with probes. The laser beam entered the chamber by port 1 after passing through a 33 cm focal length lens. Angle of incidence on the target was 30° normally but could be varied depending on angle desired. The radial distances of interest extended down to 3 mm from the end of the focal spot and probe damage at this location

is considerable. Probe tip erosion was closely observed and the probe was rotated between runs to minimize damage. Bringing the laser beam in at an angle results in an early expansion of the plasma in the direction of the reflected laser beam [2]. The main plasma however expands in the direction of the target normal.

The chamber could be pumped to a vacuum of 5×10^{-6} Torr (air) by an oil diffusion pump. For experiments requiring an ambient background for the laser produced plasma the selected gas could be admitted to the chamber. Vacuum pressures lower than 10 mTorr were measured with an ionization gauge. Higher pressures had to be measured by means of a thermocouple gauge, which was calibrated to the ionization gauge when the transition from one to the other was made.

D. TEMPORAL REFERENCE

The optical path lengths between the beam splitter and the photodiode and the beam splitter and the target are the same, therefore the time sequence is determined by the lengths of the coaxial cables connecting the components. Each cable used was tested on a Tektronix 519 oscilloscope and the cable induced delay determined from the signal transit time obtained from the scope.

Two separate reference frames for timing of the pulse were calculated, one for use with only the magnetic probe and a second for use with both the magnetic probe and the photodiode x-ray detectors. The coaxial cable (RG 58) from the photodiode to the oscilloscope was longer than the coaxial cable (RG 174) from the probe to the oscilloscope.

It was determined that the probe signal reached the oscilloscope 4 nsec ahead of the scope trigger signal, when only the magnetic probe was used. The addition of the photodiodes required a separate scope (Tetronix 7704) and a resultant time delay of 16 nsec due to the additional cable length. Figure 2 indicates the component arrangement. Zero time was established as that time at which the leading edge of the laser pulse strikes the target. The horizontal drift was checked intermittently and was observed to be negligible. A plot of the laser pulse, photodiode signal and the magnetic field from the first shot are reproduced in Figure 10 for visual comparison. The peak of the photodiode signal was not observed to change as did the peak magnetic field.

E. PHOTODIODES

Two Quantrad C50 PIN 75 double diffused silicon detector photodiodes were used to detect the x-ray emission from the laser produced plasma and from this obtain an independent determination of the plasma temperature. PIN photodiodes consist of an entrance window dead layer of .3 to 1 microns, an active (depletion) layer of 75 to 500 microns and a positive silicon layer. X-rays penetrating the absorption filters and the dead layer produce a current, by the photoelectric effect [28], proportional to the magnitude of the plasma x-ray emission, which was measured. Probe construction and use is covered by Shewchuk [31].

These two probes were introduced into the chamber from port # 5 (Figure 3) on a mounting plate designed such that each photodiode was centered to receive x-rays from the crater region of the target. Maintaining a constant -75V bias on the two photodiodes, the resultant signals were

simultaneously displayed on the Tetronix 7904 oscilloscope with an introduced time delay between signals. From the ratio of the magnitudes these two signals a plasma temperature can be estimated.

The graphs and technique to obtain this plasma temperature for the absorption filters and energies used is given in detail by Shewchuk [31].

F. MAGNETIC PROBE

1. Construction

The inductive magnetic probes used for this experiment were made from # 41 gauge copper wire. Several probes were constructed with various cross-sections, number of coil turns and methods of potting. The two complete probes utilized for this experiment were both free-standing coils with five turns of #41 gauge copper wire soldered to a copper jacketed microcoax as described by R. C. Phillips and E. E. Turner [25]. To provide for greater flexibility in later experiments the probe interior with attached stainless steel shielding and brass terminal housing were not potted into the pyrex glass tubes as in previous experiments. A neoprene connector with an o-ring fitting was glued to the bottom of the brass terminal housing which allowed rotation of the probe without disturbing the current position. This quick disconnect permitted removal of the inductive coil from a badly damaged (pitted and cracked) pyrex tube into a new tube which would maintain the vacuum while providing the proper insulation from the hot plasma. Figure 4 illustrates probe construction.

2. Calibration

Probe calibration was done by inserting the probes into a set of carefully wound Helmholtz coils and using the procedure outlined by McLaughlin [20].

The probe response must be linear in the frequency range of interest. The magnetic probes constructed were found to be linear up to a frequency of 25 MHz (Figure 5).

3. Signal Integration

The response of a magnetic probe is an induced voltage V_p which is given by [5]

$$(11) \quad V_p = nA \frac{dB}{dt}$$

where nA is the effective area of the inductive coil and dB/dt is the time rate of change of the component of the magnetic field parallel to the magnetic axis of the coil. For equation (11) to be valid it has been assumed that the magnetic flux across the face of the coil is constant.

To record a signal proportional to the magnetic field the output of the probe must be integrated with respect to time. This was done with a passive RC integrator as shown in Figure 6. V_p represents the induced voltage in the probe and V_o is the output voltage of the passive RC integrator.

Since the input is from a magnetic probe a

relationship between V_o and E can be developed with only two unknowns [5] one of which is measured.

$$(12) \quad V_o = (nA / R_i C_i) B$$

The lowest frequency f_o for which the above equation is considered valid is $2\pi f_o RC \geq 10$. If this requirement is satisfied equation (11) can be applied to any signal which has a fundamental frequency above f_o .

Frequencies encountered varied from 5 MHz to 12 MHz and the lowest rise time noted was above 20 nsec. The rise time of the probe was determined by evaluating the probe response. The calibration signal for the Helmholtz coils was sinusoidal and a rise time equal to one fourth the period was chosen. This results in a rise time of approximately 10 nsec which is shorter than any rise times encountered. The probe responses were linear for all frequencies below 25 MHz.

To satisfy the frequency restriction a time constant of $RC = 3.3 \times 10^{-7}$ sec was used. Then $2\pi f_o RC = 10.36$ assuming a frequency of 5 MHz and a time constant of $RC = 3.3 \times 10^{-7}$ sec. The conversion factor between the magnetic field and the output of the RC integrator can be obtained from equation (12). For a time constant of $RC = 3.3 \times 10^{-7}$ sec and an effective area $nA = 5.67 \times 10^{-6} \pi^2$ then

$$E[\text{Gauss}] = .58 \text{ V}[\text{millivolts}].$$

This conversion factor was recomputed each time a different probe or time constant was used.

4. Reliability

To insure meaningful data several steps were taken to evaluate each probe constructed. Several shots were taken with the probe in place but with the laser pulse blocked. Since no magnetic field was generated the trace on the oscilloscope represented electrostatic pick-up. The largest electrostatic noise obtained was less than 10 mV. This is relatively small compared to the pulses measured and therefore no effort was made to eliminate it. This check was repeated every 25 shots to monitor the effect of any extraneous signals.

After recording a signal the probe was rotated 180° and a second reading was taken. The two signals were then compared with respect to their magnitude and time of peak signal. Both signals provided the same values and the probe was considered nearly symmetric about the magnetic axis.

G. EXPERIMENTAL METHODS

All measurements taken in this research were made in an effort to determine if the presence of a crater influenced the mechanism for generation of spontaneous magnetic fields. The probe locations which offered the best indication of crater effect lay along the $Z = 1 \text{ mm}$, $\phi = 0^\circ$ radial line for

several reasons. Along this line the crater wall and laser beam were parallel to each other and perpendicular to the radial line on which the probe was located. The only other radial line for which this was true was $\phi = 180^\circ$ which was inaccessible with the probes constructed. Trends noted from these locations could be compared with similar points of previous researchers.

The magnetic probe was inserted through the port on top of the vacuum chamber and positioned in such a way that the magnetic axis of the coil was parallel to the azimuthal magnetic field lines. This location was carefully measured with respect to the focal spot of the He-Ne alignment laser. Radial distances from this focal spot varied from 3 mm to 7 mm. All magnetic probe locations were identified by cylindrical co-ordinates placed in brackets. The location $r = 5$ mm, $\phi = 90^\circ$ and $z = 2$ mm would be $(5,90,2)$. The orientation of the co-ordinate system with respect to the target and the incident laser pulse is depicted in Figure 7.

Examination of the initial trial runs indicated that the data followed a consistent pattern which did not change appreciably after 25 shots. Data runs were limited to 50 shots or less and the three preferred probe locations selected were $(3,0,1.5)$, $(4,0,1)$ and $(7,0,1)$. A brief analysis indicated that the probe location was the most sensitive parameter because the radius obtained was used to extrapolate the magnetic field back to the edge of the laser focal spot. Crater dimension analysis followed each data run.

The first traces of the time rate of change of the magnetic field were analyzed to determine the frequency range of the signal and thus select a compatible integration

time constant. Four typical dB/dt signals were traced from the poloroid pictures to show the temporal change of the pulse (Figure 8). Graphical integration of this signal showed that rc frequencies below 5 MHz were to be expected in the time frame of interest. A time constant of 3.3×10^{-7} sec was constructed for the passive RC integrator.

The addition of x-ray sensitive photodiodes provided an independent means of determining the plasma temperature. As long as the magnetic probe did not obscure the field of view of the photodiode detectors the two types of probes were compatible and provided an excellent dual measurement of the plasma. The estimated plasma temperature was obtained from computer programs developed by Shewchuk [31]. The ratios of the magnitudes are weighted, averaged then read into a computer program which then applies an iteration process to interpolated curves. The estimated general plasma temperature of 162eV was generated with an accuracy of about 10%. This value was considered characteristic of the entire plasma and was used to estimate the magnetic field intensity and focal spot radius from theoretical models.

After completing a data run the target crater was photographed on a bench metallograph using a magnification of 100. This method of measuring the crater was also considered to provide the best estimate of the focal spot size of the laser beam. A superimposed scale photographed with the crater allowed measurement to within .001 cm. Due to the random error inherent in picking the crater edge at this magnification numerous values were statistically averaged to obtain an optimal radius.

H. DATA COLLECTION ERROR ESTIMATES

1. Spatial

The magnetic probe was introduced through the top of the vacuum chamber and the position of the probe was determined by means of a grid placed behind the probe. The radial and axial distances could then be measured to within an accuracy of .5 mm. This measurement was the most critical because any error was compounded when the magnetic field was extrapolated back to the focal spot.

2. Temporal

Magnetic probe signals were measured with a time scale of 50 nsec allowing interpretation of the results to within 5 nsec. The photodiode pulse was 18 nsec FWHM and was measured on the 20 nsec scale providing an accuracy to within 2 nsec.

The vertical scales used for the magnetic probe and the photodiode detector were 500 mV and 20 mV respectively. Plexiglass overlay grids were used to interpolate values to 50 mV and 2 mV from polaroid photos of the signal trace.

3. Probe Perturbations

The probe outside diameters were initially 2.1 mm for probe 1 and 3 mm for probe 2, both values expanding to 2.3 mm and 3.2 mm respectively after coating the tip with adhesive cement to prevent leakage and retard probe damage. Probes of this size can cause disturbances in the plasma which can lead to incorrect results. Initial weak magnetic perturbations were attributed to this but the remainder of

the signal is considered relatively unaffected. The emphasis was placed on evaluating the relative value between shots which should not be influenced as much by probe induced perturbations.

V. DATA AND RESULTS

The data presented in this section are discussed and analyzed; estimates of pertinent plasma parameters are included where appropriate. General trends and observations of all data collected are discussed prior to examining data from three selected probe locations. Analysis of this data is then presented and reviewed in consideration with previously proposed plasma magnetic models.

A. OBSERVATIONS

Several characteristic trends were prominent throughout all the experimental runs totalling over 400 shots on several aluminum targets. Regardless of the radial position of the inductive probe the magnetic field strength decreased with each additional shot on the target. This type of behavior was initially suspected prior to taking any data. An unexpected observation was that the magnetic field generation mechanism appears to have two distinct phases. The first few shots produced much stronger magnetic field strengths with a shot-to-shot decrease of the peak magnetic field signal, E_{\max} , whose slope was an order of magnitude greater than the shot-to-shot decrease of E_{\max} for later shots. To characterize these two phases the steeper E_{\max} slope was called the "early shot" phase because it occurred while the target crater was relatively shallow. The more

gradual E_{\max} slope, observed as the depth of the crater base penetrated beyond the direct line of sight from the inductive coil, was named the "late shot" phase. The juncture of these two phases, called the transition point of the two stage mechanism, exhibited a shift toward lower shot numbers as the radial distance of the probe location increased. Attendant with the decrease in E_{\max} (note scale change) from shot-to-shot was an increase in the time of arrival of that peak intensity, t_{\max} , and of the arrival time of the subsequent magnetic field reversal. Figure 9 illustrates the decrease in B_{\max} for three different shot numbers at the probe position (4,0,1). Two minor features of this plot are the delay in the onset of the main plasma signal as the crater depth increased and the small early time signal (ETS) located just before the onset of the main plasma signal.

X-ray emission from the target plasma remained consistent throughout the crater excavation. In each case the peak x-ray emission from the plasma corresponded to a constant (within precision of measurement) electron temperature independent of the crater depth. Figure 10 depicts the nearly simultaneous arrival of the peak values of the laser pulse and the photodiode signal both followed by the later arrival of the magnetic field signal registered at the probe located 4 mm from the crater. The radial expansion velocity of the peak is 1.14×10^7 cm/sec.

B. CRATER DIMENSIONS

Meaningful analysis of the data collected requires detailed knowledge of the craters excavated during the investigation. Time measurements must be adjusted for the increase in path length caused by increased crater depth and all plasma magnetic field models proposed are dependent on the size of the laser focal spot. Dimensional crater surveys were conducted with a bench metallograph and a Scanning Electron Microscope (SEM). SEM micrographs were taken for all craters which could be properly sectioned for examination. These micrographs provide the most accurate method for measuring crater dimensions and estimating upper and lower bounds of the focal spot size.

Figures 11 and 12 are optical micrographs of the craters formed after firing one shot, eleven shots, forty shots and of the crater splash zone after several shots. The azimuthal wavelike pattern in Figure 12(b) appears to be deposits of molten target material splashed about the crater perimeter. The radial extent of this material measured from the micrograph of Figure 11(b) was about .560 mm. After several shots a distinct ridge of deposited material had formed at the crater's edge, Figure 12(a). The regions observed conform to the crater, splash zone and plasma-affected area noted by earlier investigators. Diameters of the crater entrance measured after one shot had an average width of .320 mm. This value is slightly larger than the .200 mm reported by Eleach and Nagel [3] for a similar irradiance. Continued crater excavation up to 65 shots at the same location produced progressively larger radii at the crater mouth with the crater throat and base remaining narrower. The rate of crater mouth expansion was obtained from a graph of crater radius versus shot number (see Figure 13) yielding a slope of .014 mm per shot. The crater base diameter did not change significantly from shot-to-shot and it typically had a shiny hemispherical

nodule of target material at its' center.

Cross-sections of the craters were examined with the SEM to provide dimensions of depth, width and for inspection of significant crater features. Figure 14(a) is a SEM micrograph of the crater formed in an aluminum target after 8 consecutive shots of 10^{12} W/cm^2 each. Figure 14(b) is a crater after 30 shots, Figure 15(a) and 15(b) show crater penetration depth following 61 and 65 shots respectively. From these figures it appears that once the laser is striking the crater wall at normal incidence a smaller hole is excavated. The diameter of the crater mouth (d_m), diameter of the crater throat (d_t), diameter base (d_b) and the crater depth (d) for various numbers of shots are listed in Table I. Figure 16 shows how these measurements were obtained.

TABLE I

CRATER DIMENSIONS

10^{12} W/cm^2 per shot

shots	d (mm)	d_m (mm)	d_t (mm)	d_b (mm)
8	.318	.472	.380	.164
30	1.452	1.056	.660	.282
61	2.363	1.912	.652	.260
65	3.217	2.136	.726	.320

The best estimate of the crater excavation rate determined from the average rate of all craters inspected is 0.055 mm/shot. This excavation rate and the dimensions listed in Table I were used whenever possible for various

calculations.

For a comparison of the laser focal spot size and the observed crater radius the spot size must be determined. The light intensity is

$$(13) \quad I_p = E / (\pi r^2 t)$$

where E is the laser beam energy, r the focal spot radius and t the pulse duration. For a carbon target irradiated by a ruby laser Mulser [21] graphically provides, Figure 17, a conversion from plasma electron temperature to light intensity for which the 140 eV measured by the x-ray photodiode detectors used in this investigation equates to an irradiance of 10^{12} W/cm². Assuming a laser energy of 8 joules, beam intensity of 10^{12} W/cm² and a pulse length of $t_p = 25$ nsec the estimate for the focal spot size diameter is .200 mm which is in rather good agreement with the extrapolation of R_c back to shot 1 of Figure 13. For the intensities used in this research (10^{12} W/cm²) K.G. Whitney and J. Davis [36] show that carbon and aluminum have similar conversion efficiencies for laser to x-ray energies allowing this approximation. Inspection shows that the crater width at the target surface after 1 shot is generally twice as large as the computed focal spot size width in agreement with Eleach and Nagel [3].

C. SELECTED DATA

1. Probe Position (3,0,1.5)

Location (3,0,1.5) provided the largest magnetic fields registered in this investigation. A peak magnetic field of over 1500 G was observed in a background of air at 2×10^{-5} Torr, a pressure well into the pressure independent region. The first few shots on the target produced magnetic fields which were double the magnitude of the magnetic fields observed from later shots. Figure 18 plots the magnetic field strength measured at the probe as function of shot number revealing two separate decreasing shot-to-shot slopes for B_{\max} . The B_{\max} per shot slope prior to shot 10, in the early shot phase, is greater than the slope observed during the late shot phase. These separate shot-to-shot slopes repeat themselves in other data runs and seem characteristic of all magnetic fields generated from target craters. Note the location of the transition point for these two phases.

One would expect that if the shot-to-shot decrease of B_{\max} was attributed solely to the magnetic field diffusion, due to the additional time required for B_{\max} to expand from a deeper crater, that the slope would be constant from shot 1 to shot 60. Since this is not true there must be an alternative explanation for the order of magnitude difference of the two slopes. The loss of the direct expansion path from the crater base to the inductive probe is a possible reason. This transition from a steeper to a more gradual slope is analyzed and discussed in the next section.

A quartz tube was utilized instead of pyrex in an effort to obtain readings at the 3 mm radial distance and to reduce probe damage. Despite this effort extensive probe tip damage was incurred after 40 shots. A pin-hole leak developed in the tube near the inductive coil which required application of adhesive cement. This increased the probe tip diameter which precluded returning the probe to the same location without obstructing the laser beam and causing significant disruption of the plasma.

2. Probe Position (4,0,1)

Numerous data collection runs were conducted at or near location (4,0,1). Probe damage at this location was considered minimal compared to (3,0,1.5) and the field of view for the x-ray photodiode detectors was clear permitting their use. For the runs conducted at this location a plasma temperature measured simultaneously with the magnetic field was obtained. The background pressure was 10^{-5} Torr.

Figures 19 and 20 show similar magnetic fields measured at the 4 mm radial distance. Higher magnetic fields were observed at (4,320,1) than at (4,0,1) due to the increased amount of energy of the laser beam in the first run. This difference in laser beam energy was also reflected in the plasma electron temperature which was 140 eV at (4,320,1) and 90 eV at (4,0,1). (It is suspected that the 90 eV observed in the last run is an under estimate because new absorber films were used for that data run and the plasma electron temperature computed was the lowest value of the 40 measurements conducted under similar conditions)

The two decreasing B_{\max} slopes are apparent in these

plots, however, the transition point has shifted left to the area of shot number 5.

3. Probe Position (7,0,1)

The probe location (7,0,1) was the largest radial distance at which data was collected. In a background of 2.8×10^{-5} Torr, a smaller magnetic field of 92 G was recorded as depicted in Figure 21. The magnetic fields here were lower than fields observed closer to the focal spot yet more noticeable was the near absence of the characteristic two phase mechanism. It appears from the gentle slope of the data that the early shot phase has vanished. The energies of the second and fourth shots of this experimental run were 1.5 times larger than the energy of the first shot. This increased energy caused higher B_{\max} values at shot two and shot four which suggests that the early shot phase is absent in Figure 21. Interpretation of the energy-normalized magnetic field strengths for this probe location shows a weak early shot phase.

D. DATA ANALYSIS

The magnetic field measurements collected were all taken in the pressure independent region below 1 Torr. This means that the relationship between magnetic field intensity and the intensity of the laser beam is functionally dependent on the conversion efficiency of laser to magnetic field energy. To determine the effect of the crater on magnetic field generation the magnetic field intensity observed at the probe was divided by the energy of the laser to remove

energy dependent fluctuations. This energy-normalized magnetic field strength, B_{\max}^* in units of Gauss/Joule, allows comparison of the magnetic fields produced by different amounts of energy which was necessary in this investigation.

If the formation of a crater has any influence on magnetic field generation then a plot of the energy-normalized B_{\max}^* as function of shot number should

graphically illustrate the effect. For 4 different probe

locations Figures 22-25 are plots of B_{\max}^* along the ordinate

and shot number along the abscissa for the magnetic fields

observed. Some of the B_{\max} fluctuations due to the

differences in laser power were removed as desired. The two

phases described earlier are apparent and each phase decreases in a linear fashion with each successive shot number. To confirm this, linear regression analysis of the data contained in the 4 Figures was performed on a HF-9810 computer. The results of this analysis were tabulated for each plot and are presented in Table II for comparison. An

order of magnitude increase in the B_{\max}^* slope can be seen in

each case where two slopes were calculated. For each set of

data points chosen a linear correlation factor was computed from the best linear fit. This correlation factor is an indication of how well the data may be represented by a straight line. Table II shows that the correlation factor was always greater than .83 and generally around .90 confirming that the linear approximation was valid. For the

probe position (7,0,1) the early shot correlation factor is misleading as it was obtained by inspection of Figure 25 and was computed using the first two points with a resultant ideal fit. Thus this early shot slope and correlation factor are subject to a different interpretation from the graphical plot. An exponential fit was tested and discarded because the estimated values were too high, particularly near the transition region from the early shot phase to the late shot phase. More elaborate exponential distributions were not considered due to the consistency of the correlation factor. The best linear fit is overplotted on Figures 22-25.

TABLE II
LINEAR REGRESSION RESULTS

location	slope [G/J]		correlation	
	early	late	early	late
(3,C,1.5)	-13.16	-.47	.95	.93
(4,320,1)	-5.54	-.59	.85	.91
(4,C,1)	-5.80	-.77	.96	.83
(7,C,1)	-1.38	-.81	1.0	.85

A secondary result noted from these linear fits is a better estimate of the transition point and the shift of that point to lower shot numbers as the radial distance increased. Several factors contribute to the slope of E_{\max} from shot-to-shot. The increase in crater depth causes an

an inverse-square decrease per shot at 3 mm radius of 4%. For ten shots this predicts a value of 1100 G at the 10 shot point of Figure 18, compared with the measured 625 G. This shows that the inverse square magnetic field loss cannot account for the steepness of the slope nor for the change in the transition point location.

The diffusion of the self-generated magnetic fields is controlled by the term $(1/\mu_0\sigma) \nabla^2 B$ in equation (4). Then the diffusion time is

$$(14) \quad t_d = \mu_0 \sigma L^2$$

where L is the average characteristic length of flow. Figure 9 provides the information to determine L . The e-folding time for the increase of the magnetic field in Figure 9 is 35 nsec and the expansion velocity is 1×10^5 m/sec making $L = 3.5 \times 10^{-3}$ m. For adiabatic expansion of the plasma into a vacuum ($T \propto V^{-2/3}$) following laser cut-off, a plasma temperature of 12 eV at $r = 4$ mm was determined from the 140 eV plasma electron temperature measured by the x-ray photodiodes. This plasma temperature results in a Spitzer resistivity of 1.24×10^{-4} Ohm-m and in conjunction with L yields a diffusion time

$$t_d = 150 \text{ nsec}$$

a time much longer than the time for the plasma to travel the additional single shot distance from a deeper crater. This means that diffusion does not contribute to the

a time much longer than the time for the plasma to travel the additional single shot distance from a deeper crater. This means that diffusion does not contribute to the decrease of B_{\max} from shot-to-shot.

A second more direct diffusion time was calculated from the late shot phase values of B_{\max} from Figure 19 and from the average shot-to-shot change of B_{\max} arrival time. The magnetic field relation is

$$(15) \quad B = B_0 \exp\{-t/t_d\}$$

where t is the time difference between the observation of B_0 and B . Expressing the exponential as a series expansion and then neglecting the higher order terms, the diffusion time can be expressed as

$$(16) \quad t_d = t \{B_0 / (B_0 - B)\}.$$

For a ten shot interval $t = 5$ nsec and the magnetic field changes from $B_0 = 173$ G at shot number 10 to $B = 141$ G at shot number 20. Substituting these values into equation (16) gives $t_d = 27$ nsec - a diffusion time much less than the previous one.

In close it appeared to require more shots to reach the transition point than it did at greater radial distances. This transition point could just be determined from the data at probe position (7,0,1) implying a possible loss of the mechanism which generates the larger magnetic fields. The loss of the direct expansion path from the crater to the

for the shift of the transition point to a lower shot number. Figure 26 is a scaled graphic representation of the probes at their data locations and of the angle subtended by the line of sight (LOS) from the inductive coil to the center-line of the crater. Probes located at smaller radial distances clearly have a better field of view of the plasma in the crater and would subsequently measure the higher magnetic field strengths for a longer period of shots. As the crater deepens the LOS is obstructed and the plasma can no longer expand directly to the probe. This cut-off would occur earlier for greater radial distances causing a shift of the place of LOS obstruction to a lower shot number. Therefore the geometry of the crater and the loss of LOS from the plasma could account for the shift of the transition point of the two phases.

The mechanism causing the more rapid loss of the magnetic field strength from shot-to-shot during the early shot phase could be associated with the loss of LOS also. Since the crater gradually obstructs the expansion LOS of the plasma it could reduce an early fast propagating front as well thereby increasing the shot-to-shot magnetic field loss measured at the probe. When the crater is deep enough so that no fast propagating front or other mechanism can be seen by the probe, then the shot-to-shot loss at the probe will not be as great. The mechanism itself has not been identified but the geometrical explanation agrees with the features of the data obtained from the plots.

The early shot phase then is the probable combination of two mechanisms one of which is being influenced by the crater depth up to the transition point where it is completely cut-off. From the transition point on, the secondary mechanism continues unaffected by any change in crater depth, producing a more gradual shot-to-shot decrease of the magnetic field strength.

crater depth, producing a more gradual shot-to-shot decrease of the magnetic field strength.

The magnetic fields generated at the edge of the focal spot can be calculated from equation (8). For a radial distance of 4 mm from the focal spot a magnetic field strength of 470 G was measured concurrently with an x-ray emission corresponding to a plasma electron temperature of 140 eV. Assuming $V_0 = 10^7$ cm/sec, $r_0 = 0.2$ mm then the magnetic field at the edge of the focal spot is 66.4 kG.

Assuming conservation of flux, $B \pi r^2 = \text{const.}$, the observable field at 4 mm should be 166 G, which is lower than but the same order of magnitude as the actual field measured. This model predicts a magnetic field of 54 G at a radial distance of 7 mm compared to the inductive probe reading of 92 G at that location.

Magnetic field measurements from probe position (3,0,1.5) were taken prior to the availability of the x-ray photodiode detectors and therefore a specific plasma electron temperature for this data run is not available. The magnetic field measurement observed at this location can be scaled back to the focal spot edge by assuming conservation of flux and knowing that diffusion is negligible. For this calculation the focal spot radius was obtained by extrapolating the plot of R_m back to shot 1 on Figure 13 yielding a value $r_0 = 0.11$ mm. This value is considered to be the lower bound on the focal spot size for this investigation. For a magnetic field of 1.54 kG at

probe position (3,0,1.5) the magnetic field at the edge of the laser beam would be 1.1 MG, a value in the range predicted by computer simulations of laser plasma dynamics.

Inspection of the values of B_{\max}^* for shot number 10 at different radial distances shows a decrease in B_{\max}^* as the radial distance increases. In close at 3 mm Figure 22 indicates a B_{\max}^* of 75 G/J, at 4 mm Figures 23 and 24 show 25 G/J and cut at 7 mm Figure 25 has 5 G/J resulting in comparative ratios of 15:5:1.

Figure 27 represents the arrival times of the peak magnetic field, B_{\max} , as a function of the shot number for the location (4,0,1). Since the magnetic field is convected with the laser produced plasma then the time differential between the arrival of the peak magnetic signal from shot to shot combined with the additional path length traveled by the plasma permits analysis of the expansion velocity of the plasma. The slope computed from the data on this graph and the rate of target excavation presented earlier allow a rough determination of the plasma expansion velocity inside the crater. The rate of target excavation for this investigation was 5.5×10^{-3} cm/shot and the change in B_{\max} arrival time increases 0.48 nsec/shot, therefore the plasma expansion velocity in the crater is 1.14×10^7 cm/sec. This

is a reasonable result and agrees well with the axial expansion velocities measured outside the target crater. This means that the crater does not slow down the plasma in the axial direction.

The radial expansion velocity at the surface of the target after the first shot was computed from the arrival times of E_{\max} at different radial distances. B_{\max} arrived at

(4,0,1) at $t_{\max} = 90$ nsec and at (7,0,1) at $t_{\max} = 120$ nsec.

This means that the radial velocity component of plasma

expansion is 1×10^7 cm/sec and in conjunction with the axial plasma velocity determined by Callahan [7] shows an isotropic distribution. Callahan did not observe any change in axial velocity with increased crater depth whereas this data shows a possible crater depth influence on the radial velocity component. For the same probe locations as above the radial expansion velocity was calculated from a crater developed by 10 laser shots revealing a slower radial expansion of 6.5×10^6 cm/sec, a reduction of 35%. A possible asymmetric velocity distribution has developed from the physical constriction of the laser plasma by the crater.

The mass of the ablated aluminum target material was determined by careful measurement of the crater from a SEM micrograph. The cavity examined reveals that 4.13×10^{-3} cm³ of Al were excavated which represents a total of 2.5×10^{20} atoms or 3.83×10^{16} atoms per laser pulse.

VI. SUMMARY

A. CONCLUSIONS

The formation of a crater by repeated irradiation of the same spot influences the measured magnitude of the magnetic fields caused by non-colinear temperature and density gradients. Plots reveal that the measured E_{max} for a given probe position is dependent on crater depth. The spontaneously generated magnetic fields and the energy normalized magnetic fields both display a two phase mechanism as a function of crater depth which have been divided into the early shot phase and the late shot phase. The early shot phase has a B_{max} decrease per shot which is an order of magnitude higher than the decrease of E_{max} in the late shot phase. The transition point between the two phases shifts to a lower shot number on the data plots for an increase in radial distance of the probe indicating a possible loss of the mechanism which produced the larger magnetic fields. The proposed reason for this phase change and the shift of the transition point to a lower shot number is the loss of the direct expansion path of the laser plasma from the crater to the magnetic probe.

Crater depth influence is also observed in the plasma plume radial expansion velocities determined from the time and path differences. The radial expansion velocity

decreased from 1×10^7 cm/sec to 6.5×10^6 cm/sec as the target crater depth increased from 0 to .55 mm. Since Callahan did not observe any decay in the axial plasma plume expansion velocity, the physical constriction by the crater appears to produce an anisotropic plasma plume velocity distribution. The axial velocity appeared to remain the same independent of the crater depth. This is an indication that there may be more axial directivity to the plasma exiting from a crater.

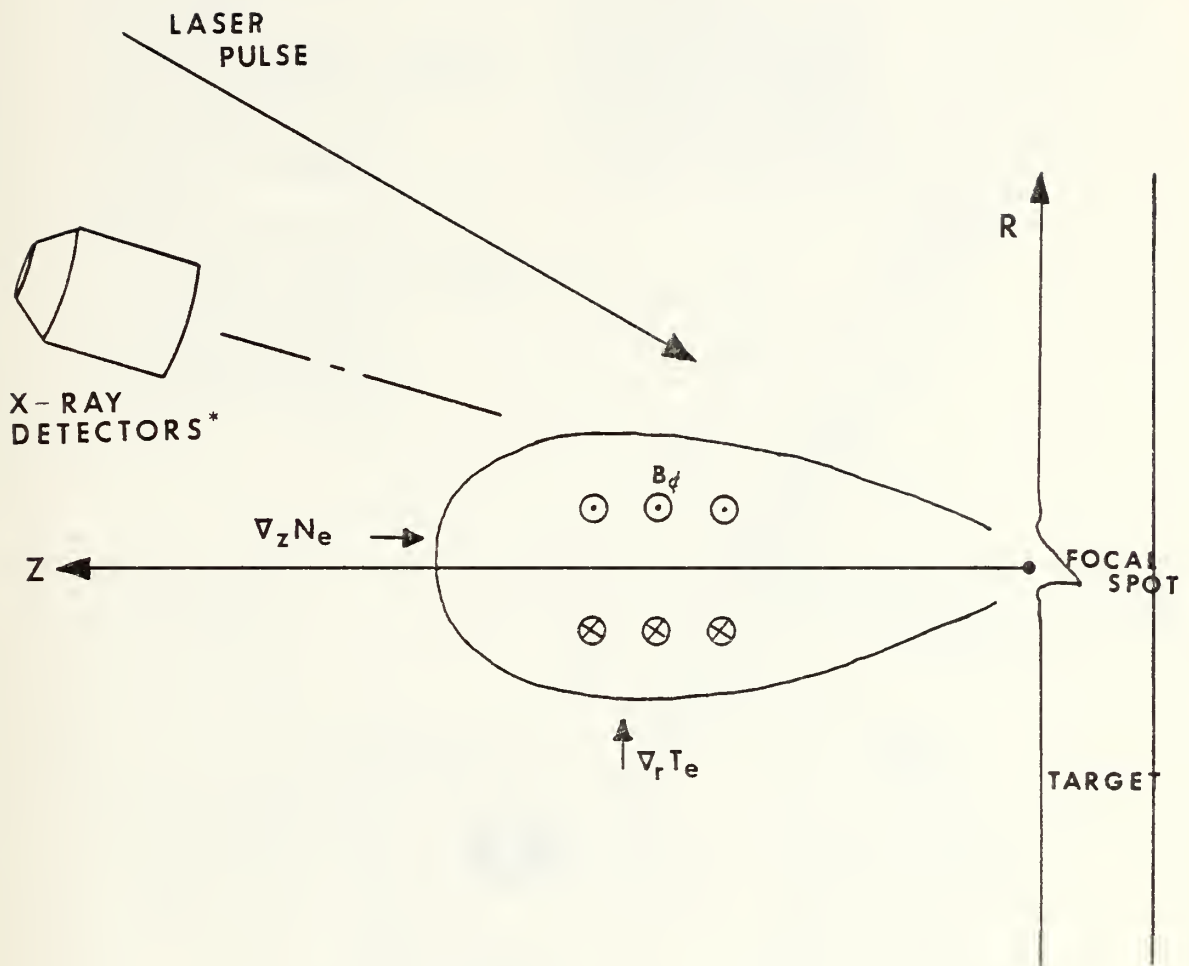
B. PROPOSALS FOR CONTINUED RESEARCH

This investigation has revealed a crater depth dependence of the magnetic fields generated in a laser plasma but more detailed experimentation is required to adequately understand their generation and propagation. The addition of plasma x-ray diagnostics at the Naval Postgraduate School provides an excellent independent information source that is compatible with both inductive and Langmuir probe probes. This diagnostic technique will provide spatial and temporal measurements with which to interpret simultaneously collected magnetic field data in future plasma research.

Development of a larger data base for crater influenced magnetic fields is needed for radial positions out to 1 cm and for azimuthal positions of 90° , 180° and 270° . In conjunction with this, a variation of the angle of incidence of the laser pulse is recommended. These results could be correlated and compared to the findings in this

investigation to confirm and characterize the two stage mechanism which generates the magnetic fields. Possible anisotropic velocity distributions could also be investigated.

It was apparent during this investigation that the passive RC integrator is a useful labor saving tool yet much of the detail present in dB/dt signals is smoothed over by the integration process. The development of a compartmentalized diagnostic computer program to digest, analyze, fit and plot the voluminous amount of data obtainable from the three types of probes available would accelerate data compilation, retrieval and interpretation at the Naval Postgraduate School.



* second detector behind one shown

Figure 1 - CONCEPTUAL PLASMA REPRESENTATION AND THE ORIENTATION OF THE TWO X-RAY PHOTODIODE DETECTORS

- | | |
|-------------------------|---------------------|
| A-Nd Amplifier Laser | N-X-ray Photodiodes |
| B-Beam Expansion Optics | O-Magnetic Probe |
| C-Nd Oscillator Laser | P-Target |
| D-Polizer | Q-Chamber |
| E-Pockels Cell | R-Rotation Knob |
| F-CW Alignment Laser | S-Scope Trigger |
| G-PIN Diode | T-X-ray Signal |
| H-Trigger Diode | U-Magnetic Signal |
| I-MgO Diffuser | V-Beam Splitter |
| J-Lens | |
| K-Tetronix 564B | |
| Storage Oscilloscope | |
| L-Tetronix 7904 | |
| Oscilloscope | |
| M-Tetronix 7704 | |
| Oscilloscope | |

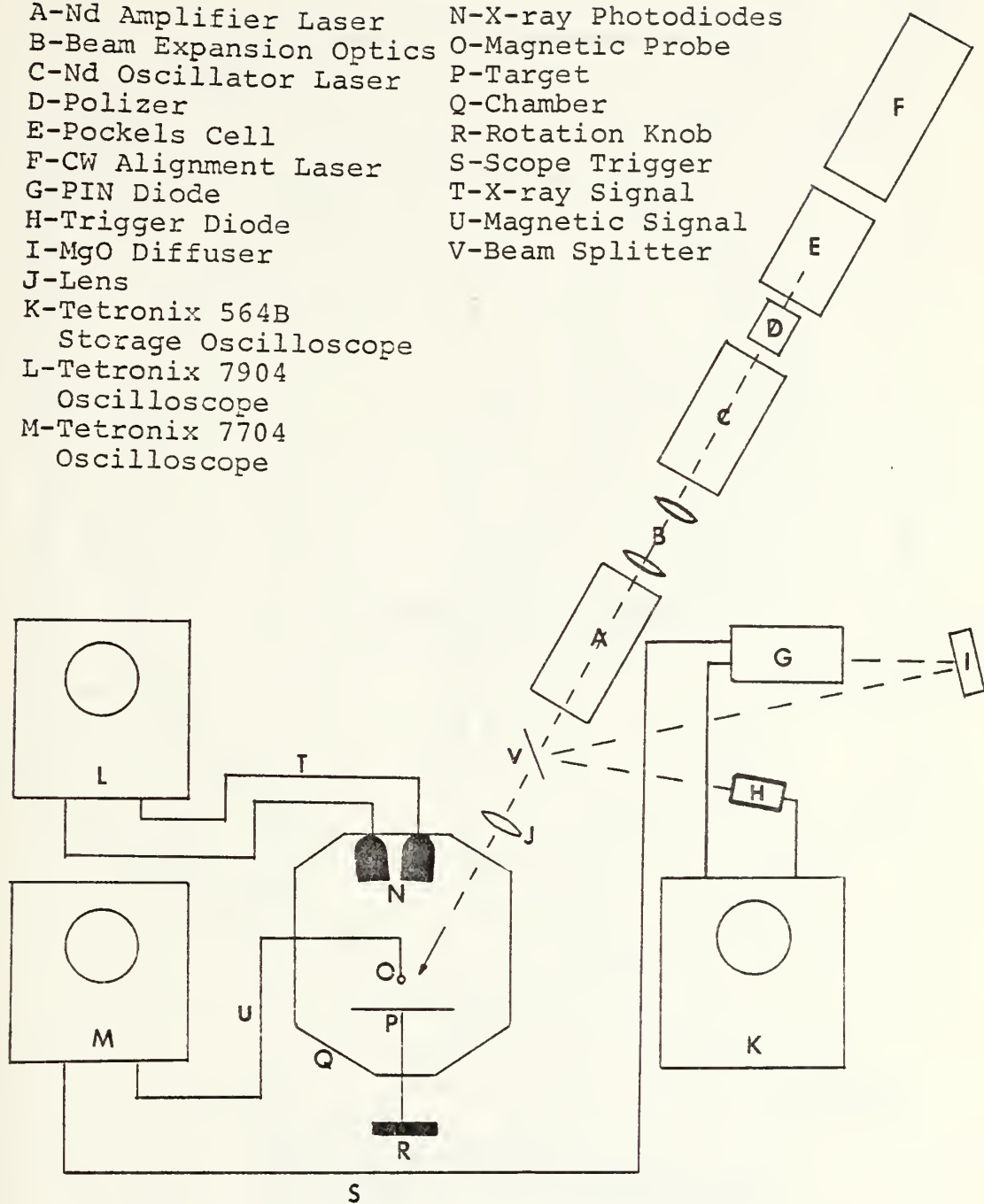
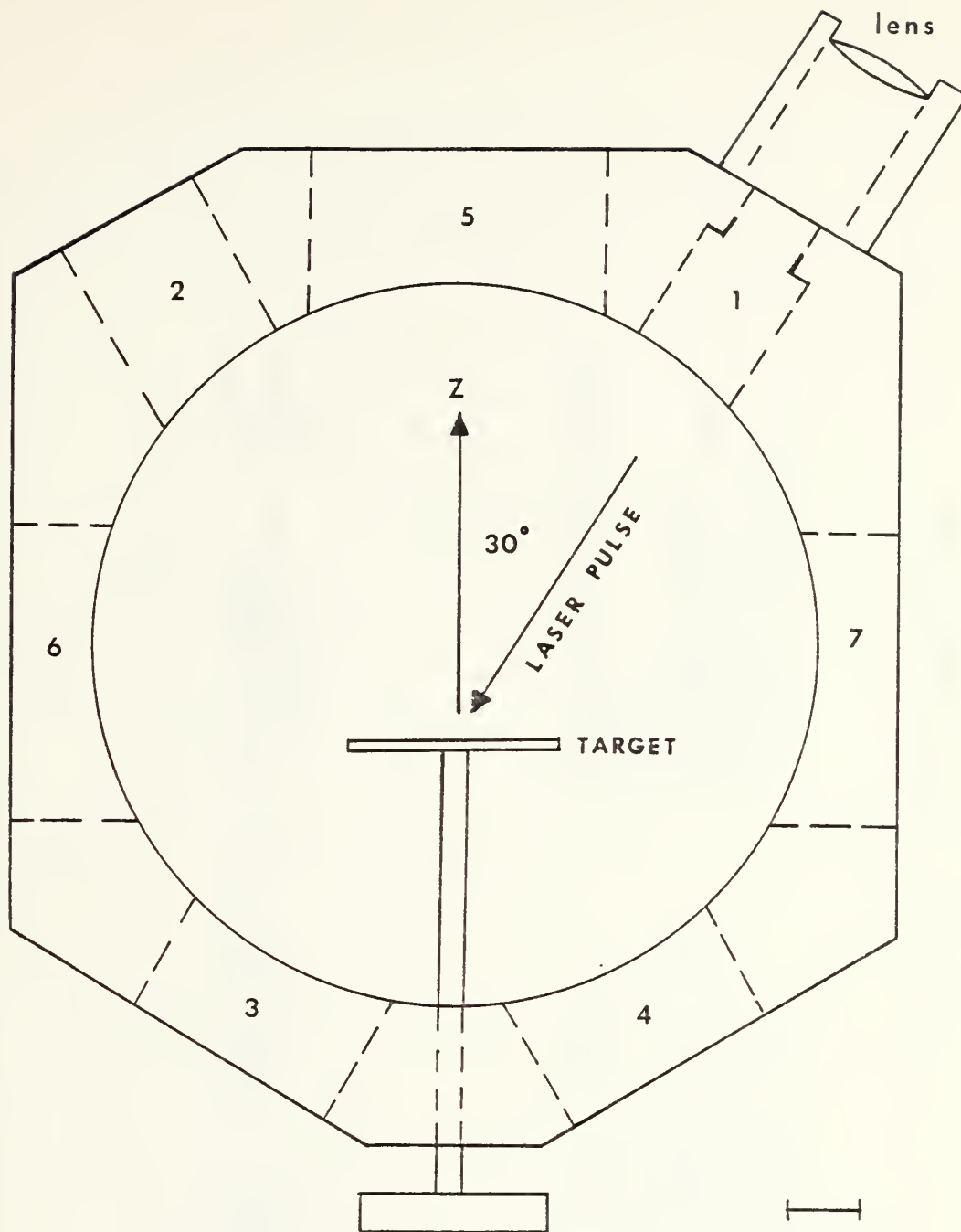


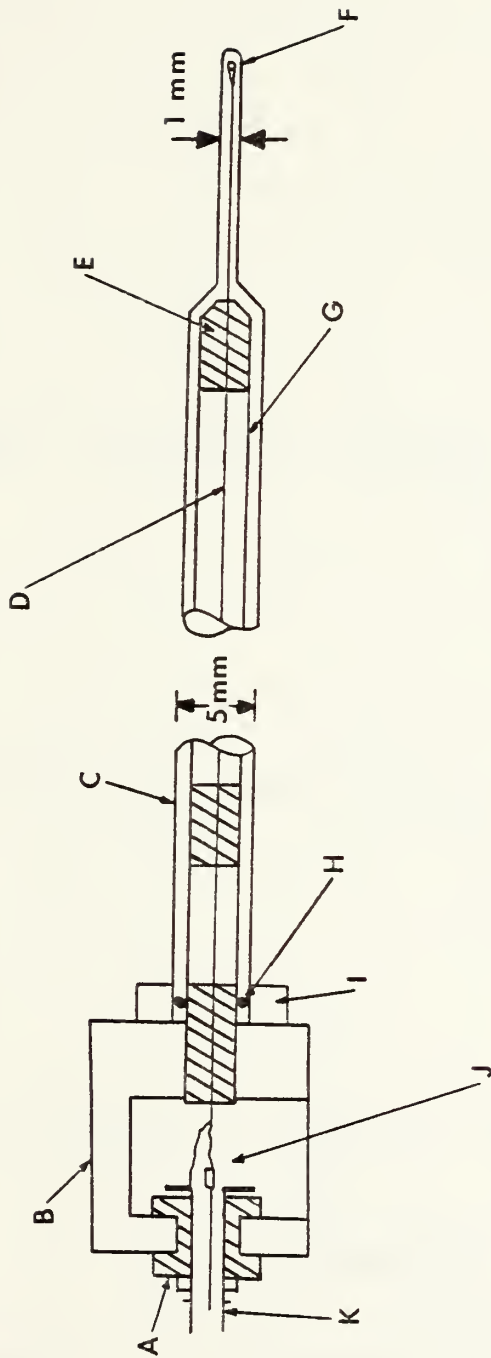
Figure 2 - LASER SYSTEM ARRANGEMENT AND EXPERIMENTAL SET-UP



- 1-Laser entry port
- 5-X-ray Photodiode port
- Top-Magnetic Probe entry port

2.54 CM

Figure 3 - VACUUM CHAMBER (TOP VIEW)



- A-Insulating bushing
- B-Brass fixture clamped to support tube
- C-Pyrex support tube
- D-Copper jacketed microcoax $Z_0 = 50$ Ohms, OD = .058 cm
- E-Nylon spacer
- F-5 turn #41 wire coil

- G-Stainless steel support tube
- H-O-ring
- I-Neoprene collar
- J-Soldered connections
- K-Amphenol 27-9 subminax connector

Figure 4 - PROBE CONSTRUCTION

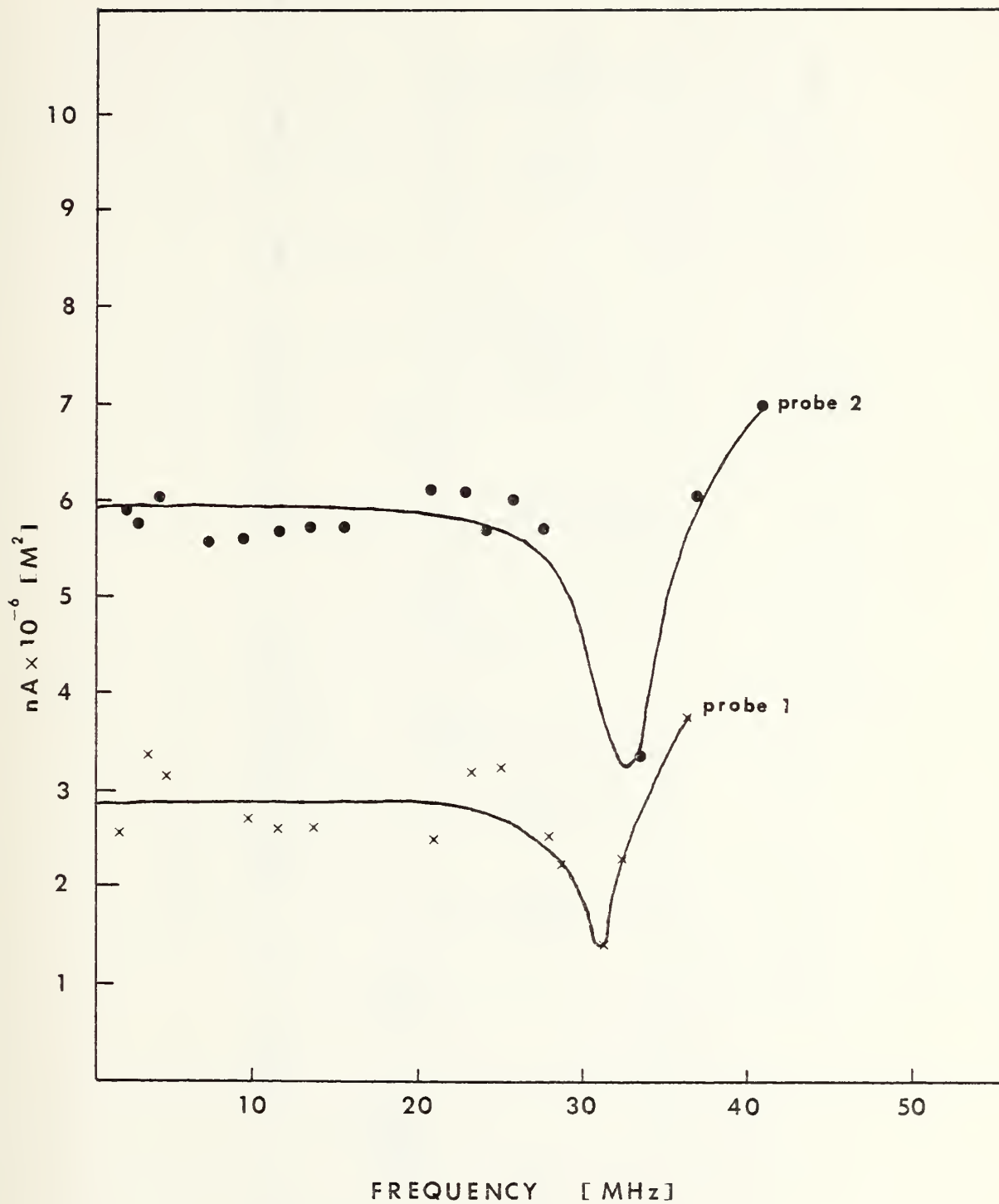


Figure 5 - CALIBRATION CURVES FOR MAGNETIC PROBES

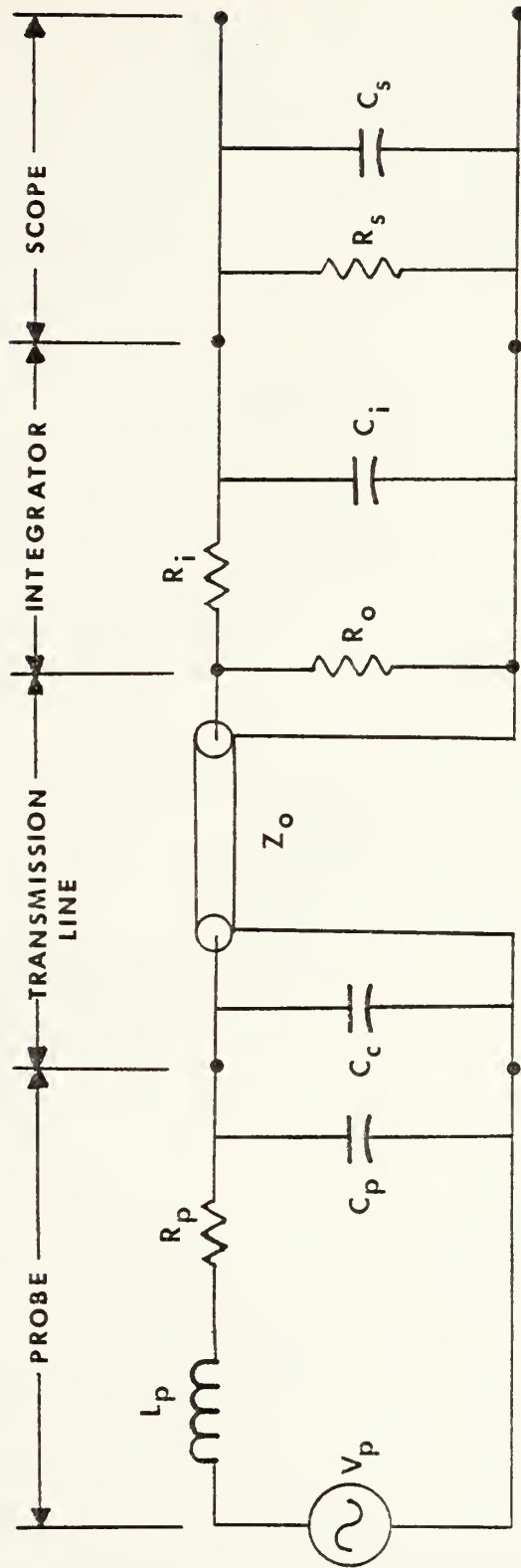


Figure 6 - CIRCUIT DIAGRAM FOR THE PASSIVE RC INTEGRATOR AND THE MAGNETIC PROBE

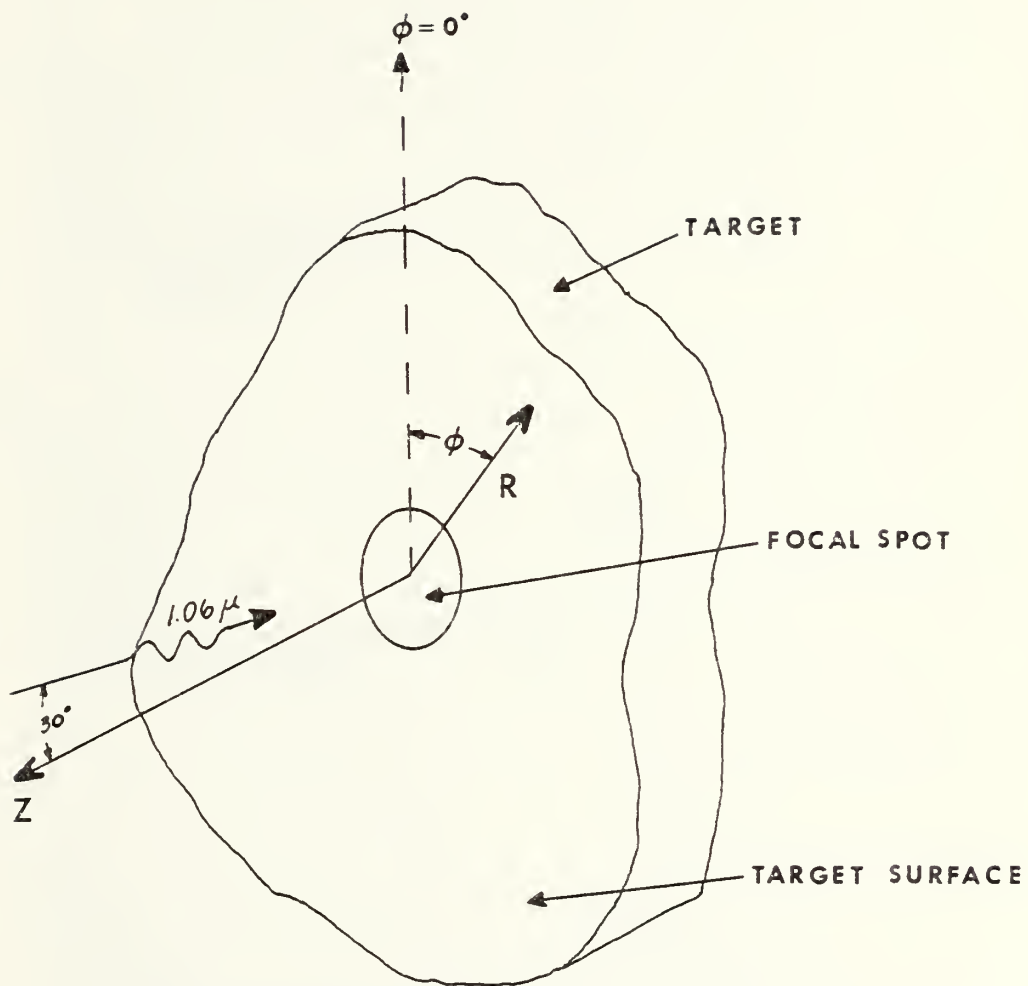


Figure 7 - CYLINDRICAL POLAR COORDINATE SYSTEM ORIENTATION

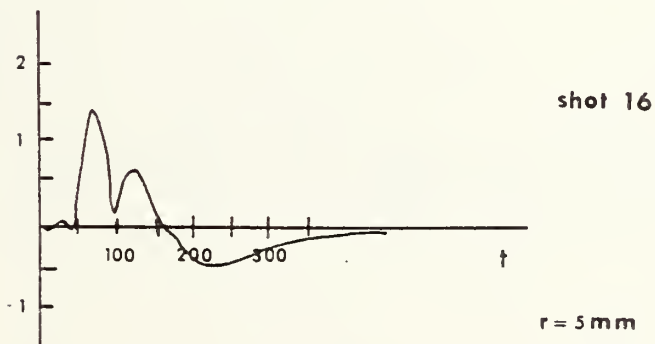
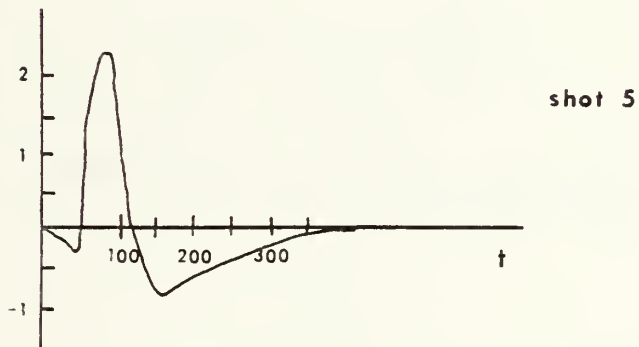
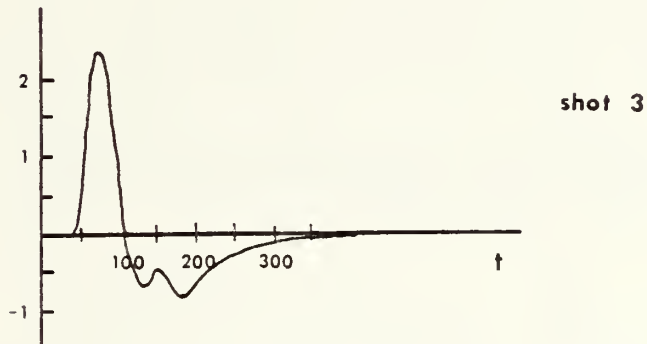
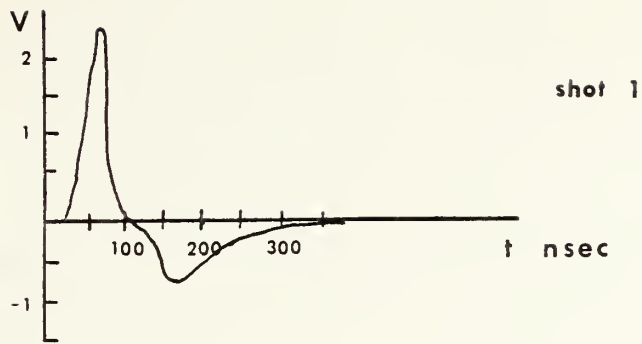


Figure 6 - MAGNETIC FIELD TIME RATE OF CHANGE SIGNALS FOR SHOTS 1, 3, 5, AND 16

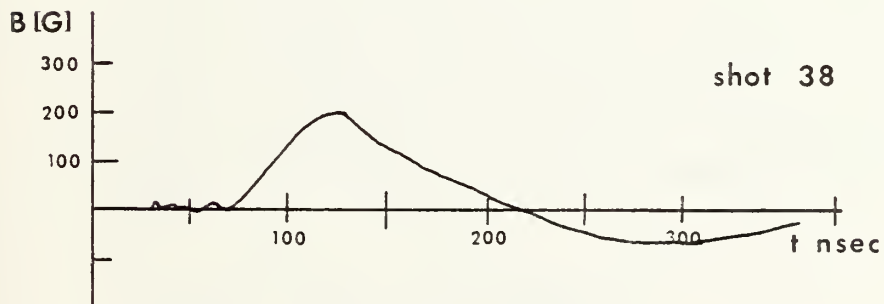
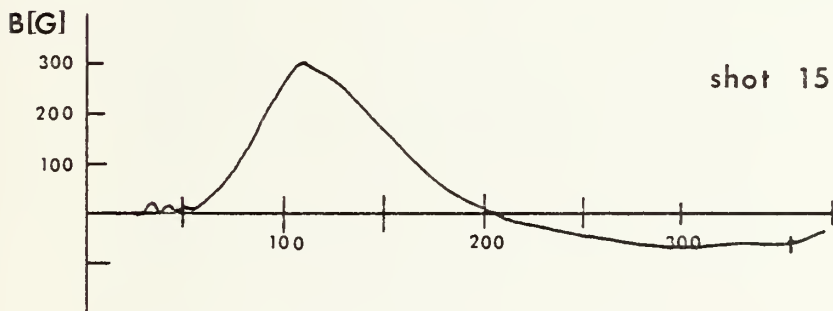
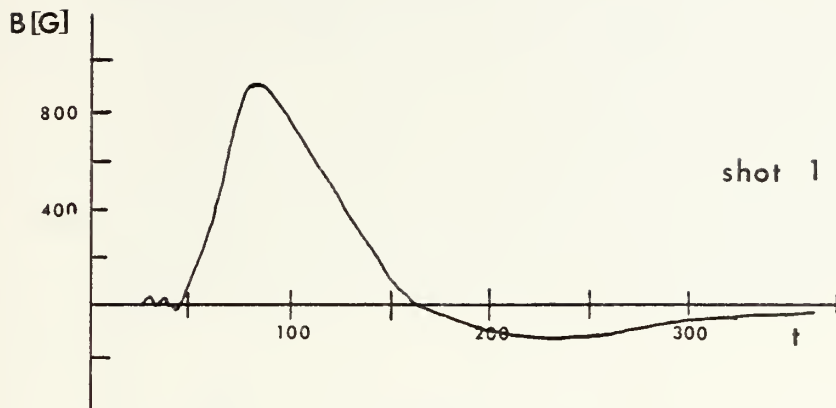


Figure 9 - MAGNETIC FIELD SIGNALS FOR SHOTS 1, 15 AND 38 AT PROBE POSITION (4, 0, 1)

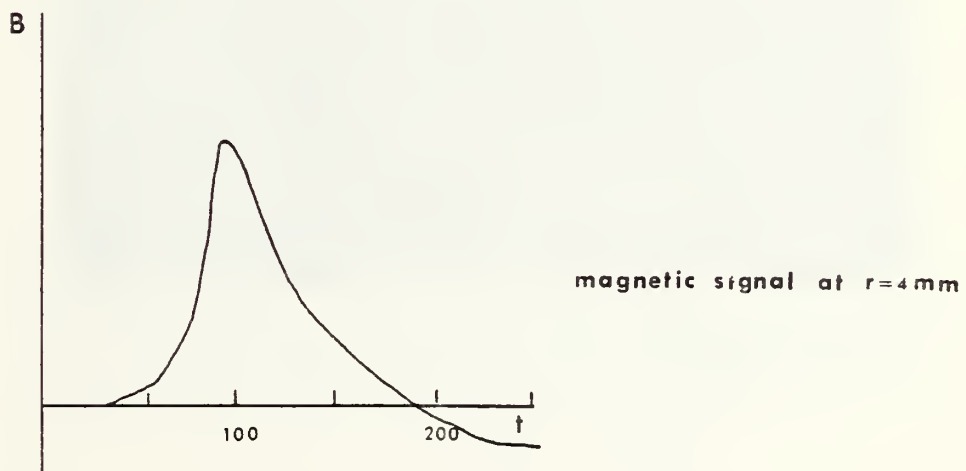
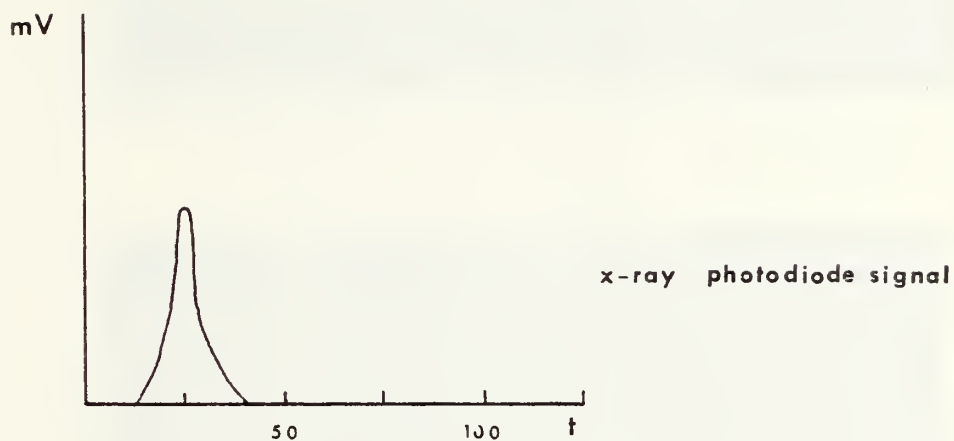
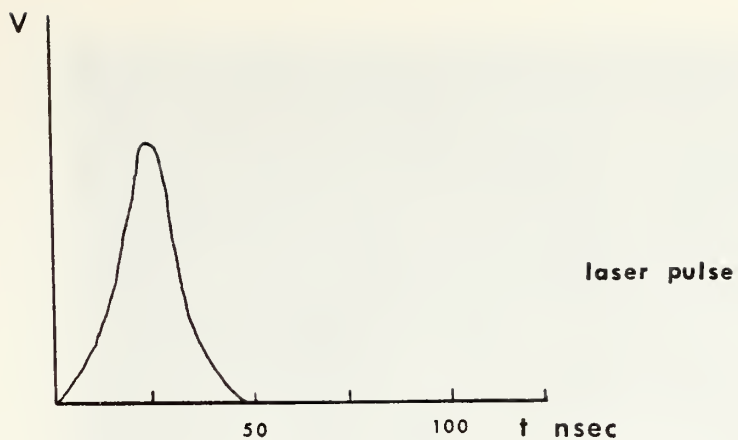
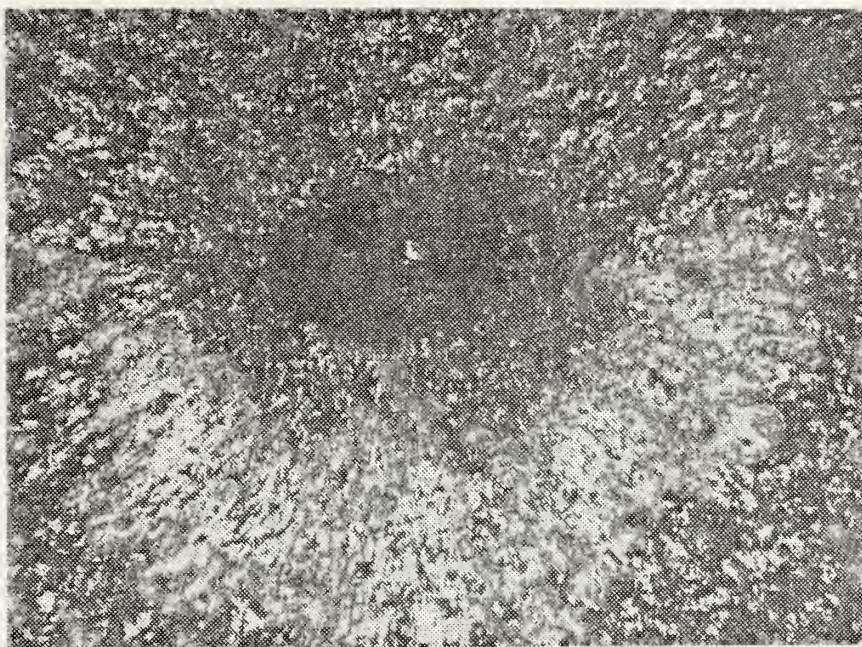
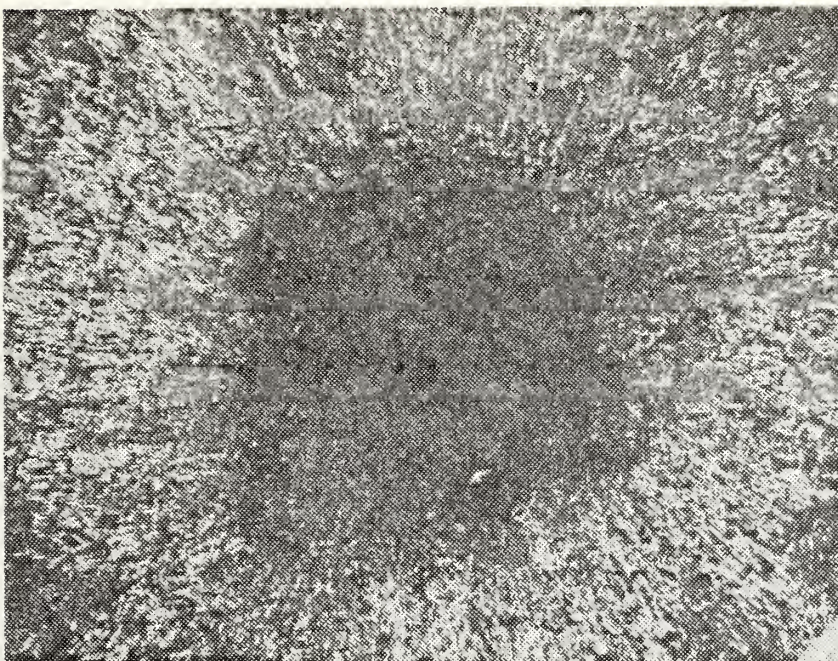


Figure 10 - TEMPORAL SEQUENCE OF LASER, X-RAY PHOTOELECTRODE AND MAGNETIC FIELD SIGNALS FOR PROBE POSITION (4,0,1)

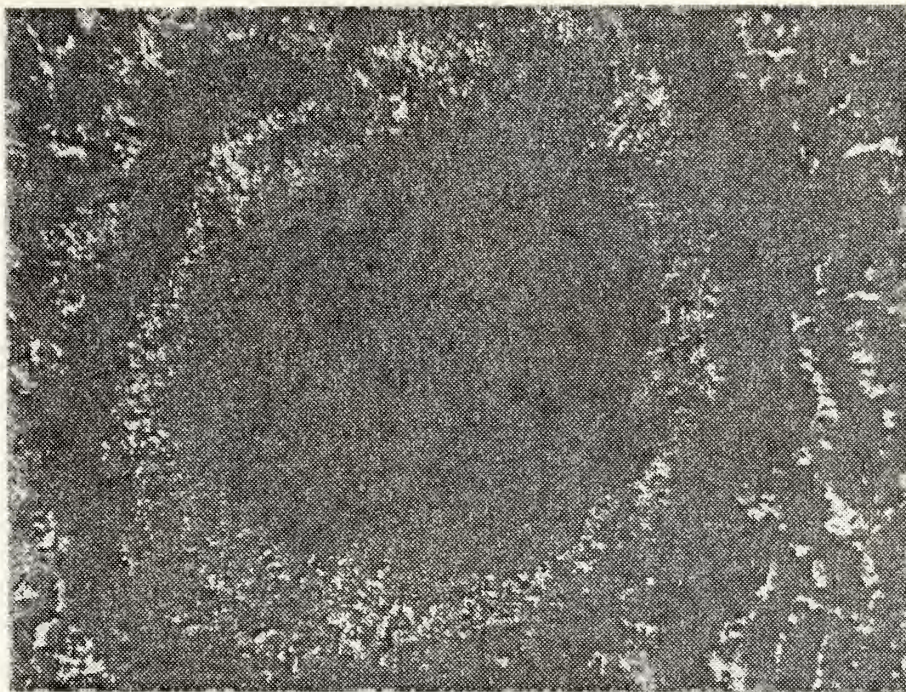


(A) CRATER MOUTH AFTER 1 SHOT (X100)



(B) CRATER MOUTH AFTER 11 SHOTS (X100)

Figure 11 - OPTICAL MICROGRAPH OF ENTRY HOLE IN AL TARGET
FOR SHOTS 1 AND 11



(A) CRATER MOUTH AFTER 40 SHOTS (X80)



(B) CRATER SPLASH ZONE (X80)

Figure 12 - OPTICAL MICROGRAPH OF ENTRY HOLE IN AL TARGET FOR SHOT 40 AND OF THE CRATER SPLASH ZONE

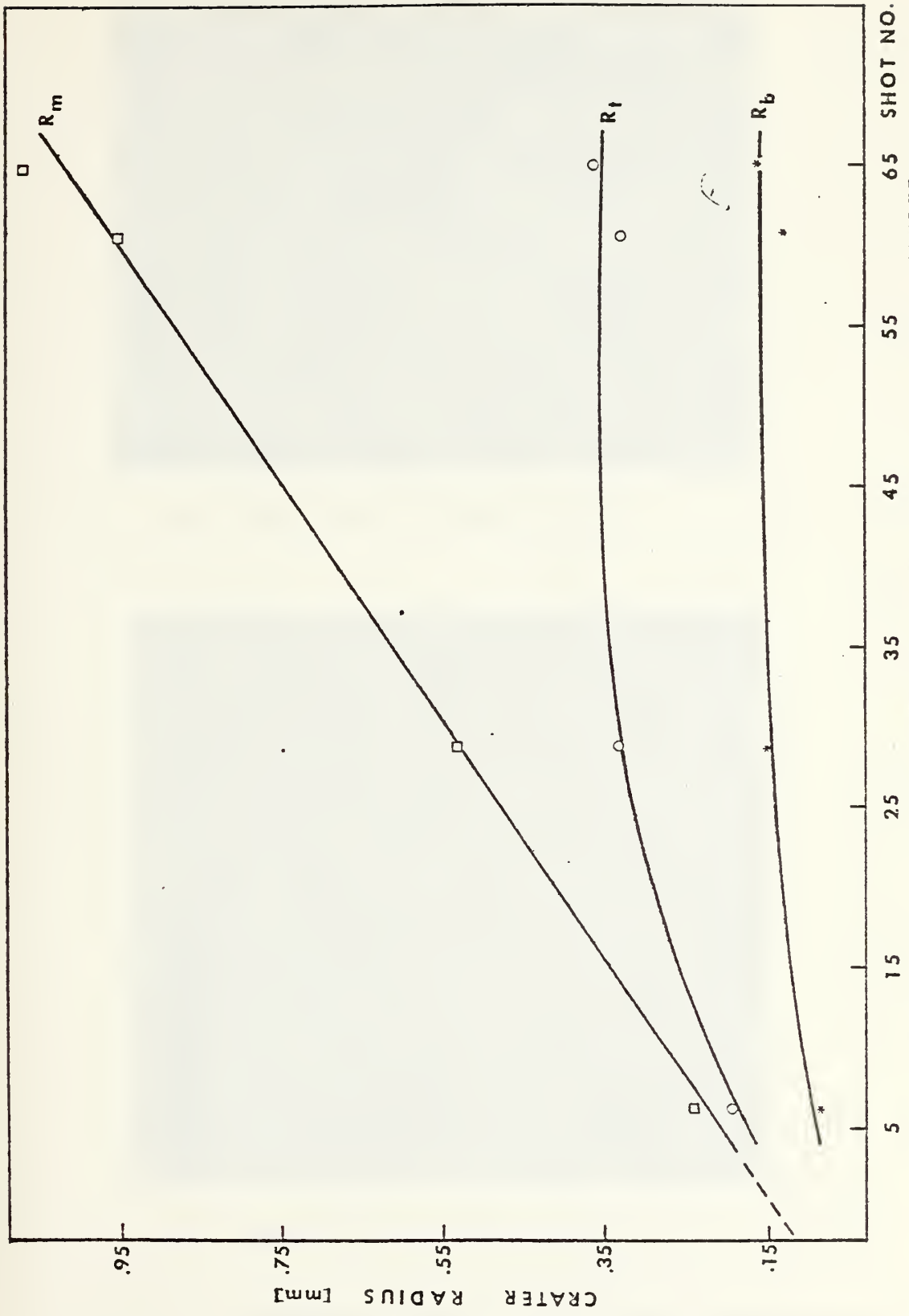
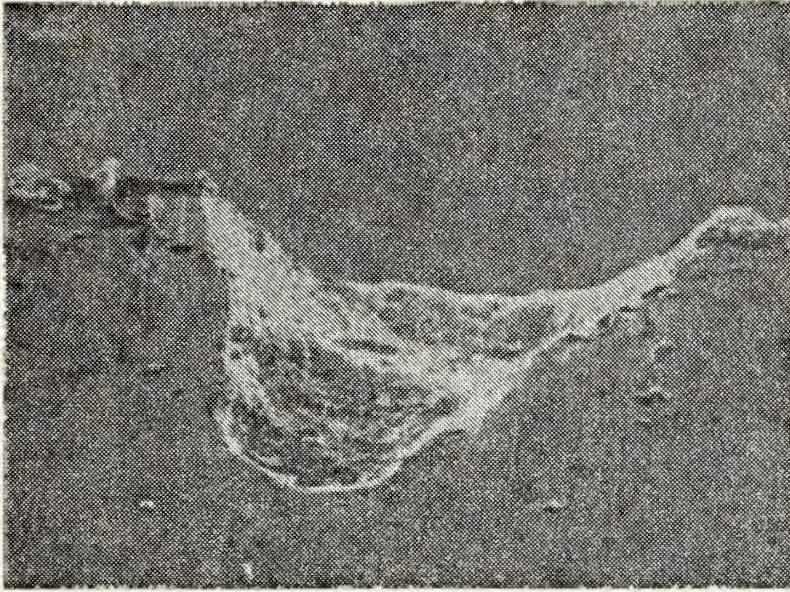


Figure 13 - CRATER RADIUS AS A FUNCTION OF SHOT NUMBER



(A) EIGHT SHOT CRATER (X110)

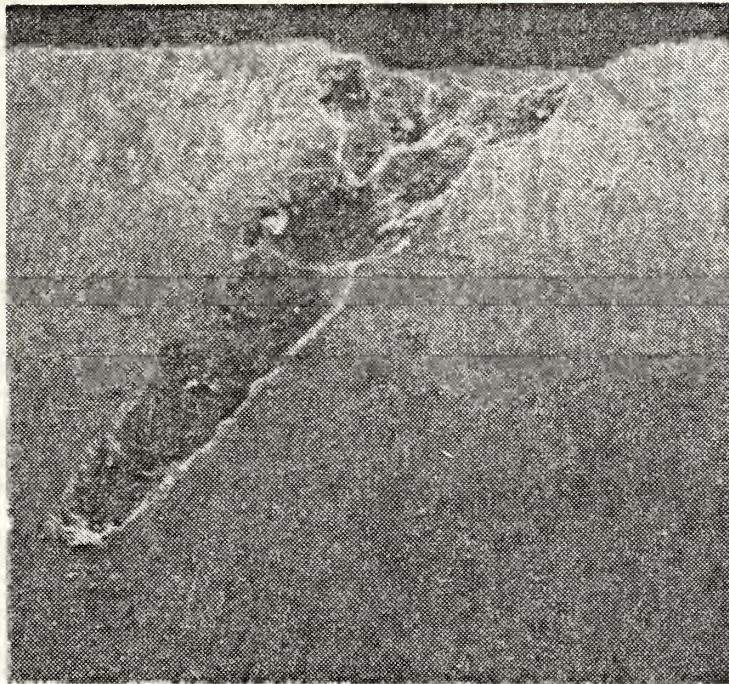


(B) THIRTY SHOT CRATER (X53)

Figure 14 - SCANNING ELECTRON MICROSCOPE PHOTOGRAPH OF A
CRATER BURNED INTO AN AL TARGET AFTER 8 AND 30 SHOTS



(A) 61 SHOT CRATER (X22)



(B) 65 SHOT CRATER (X23)

Figure 15 - SCANNING ELECTRON MICROSCOPE PHOTOGRAPH OF A CRATER BURNED INTO AN AL TARGET AFTER 61 AND 65 SECTS

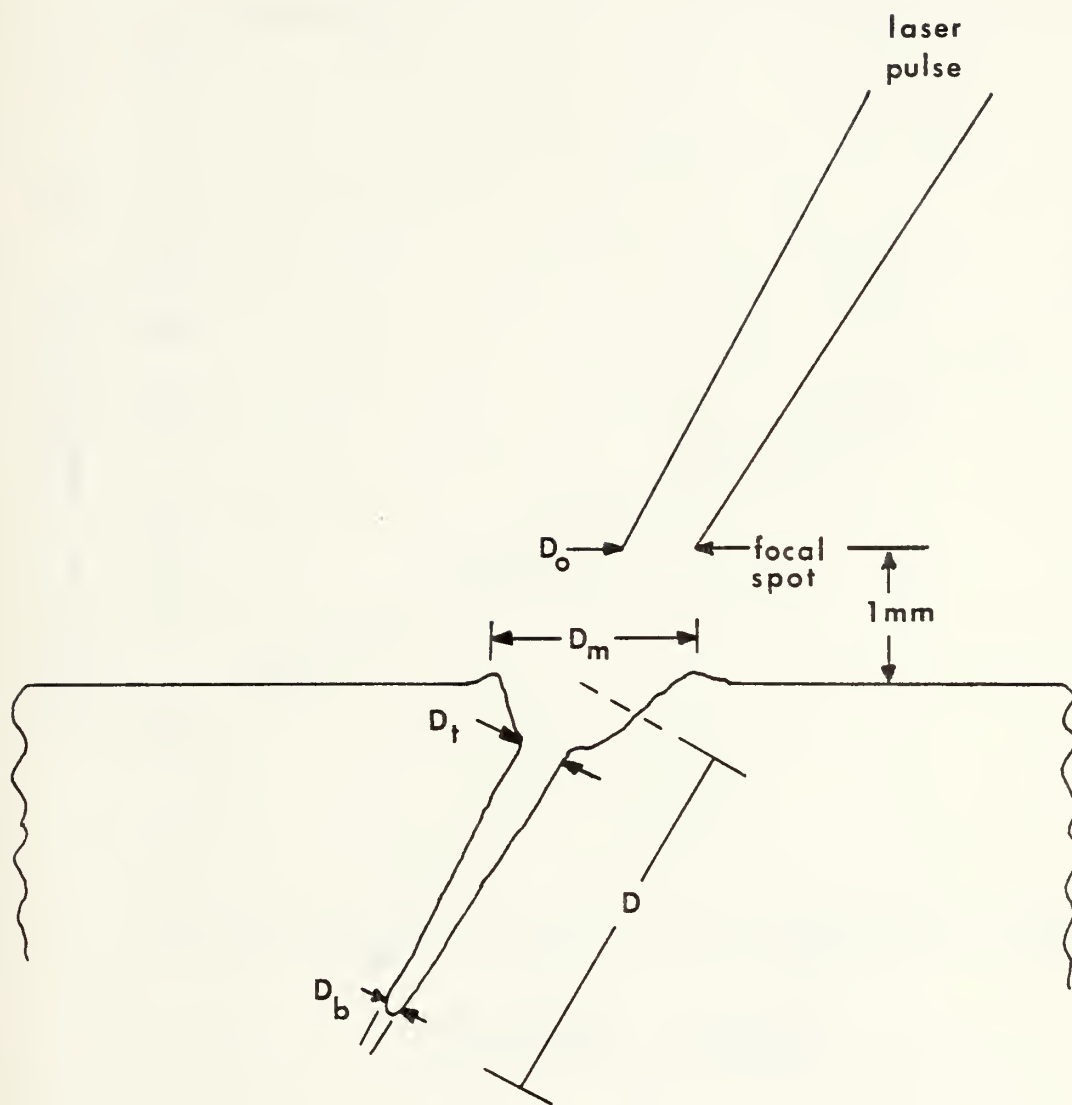


Figure 16 - GRAPHICAL REPRESENTATION OF HCIE EXCAVATED INTO THE TARGET

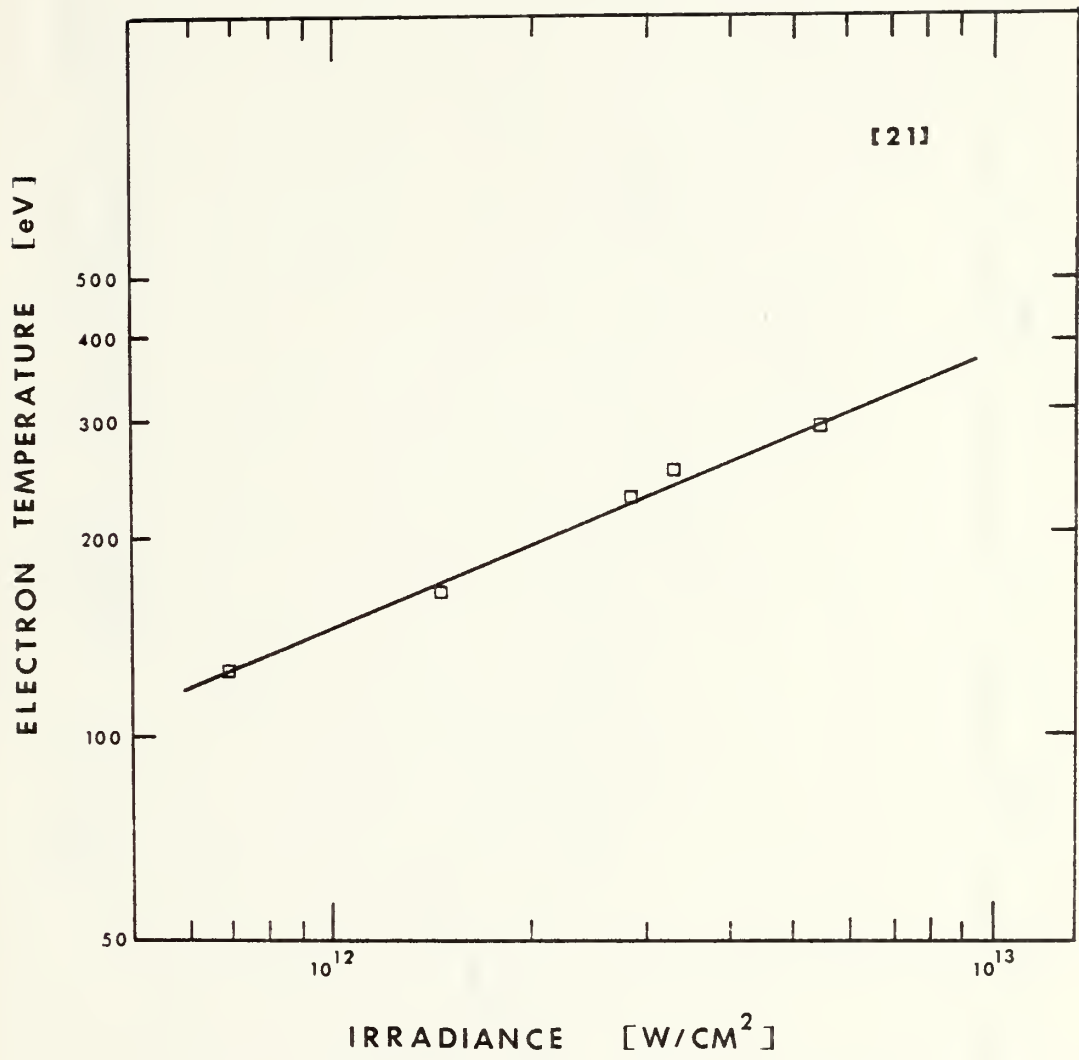
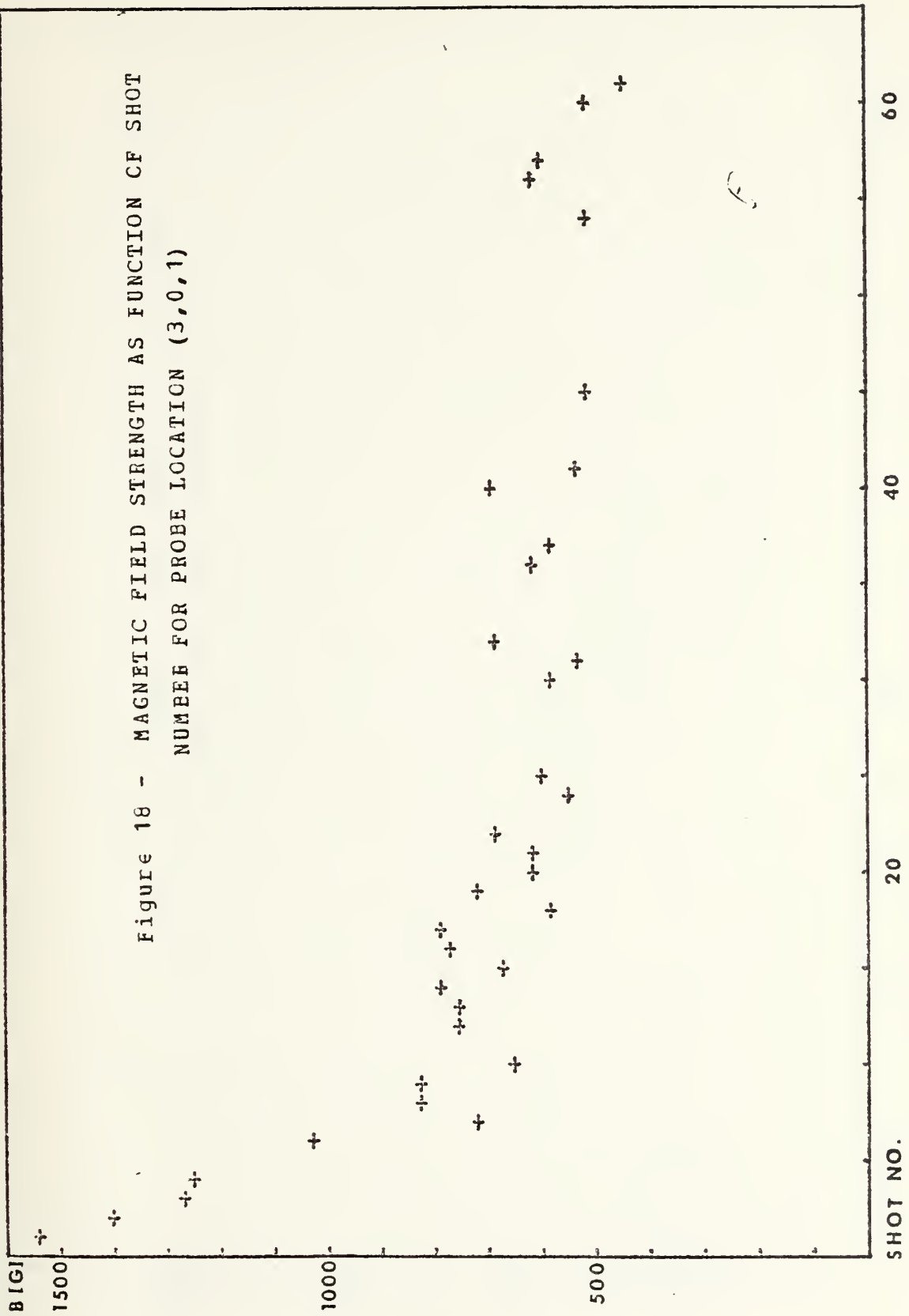
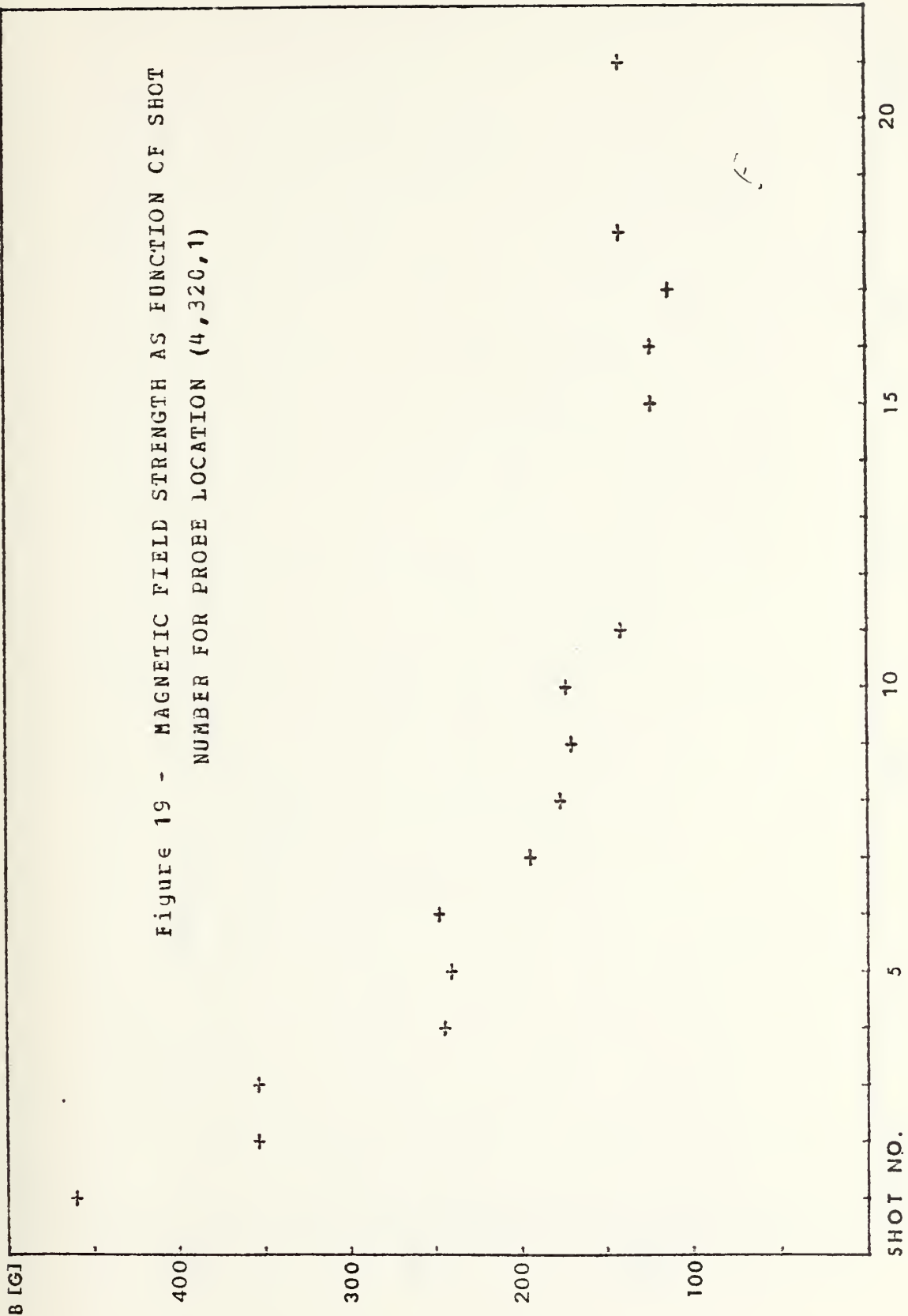
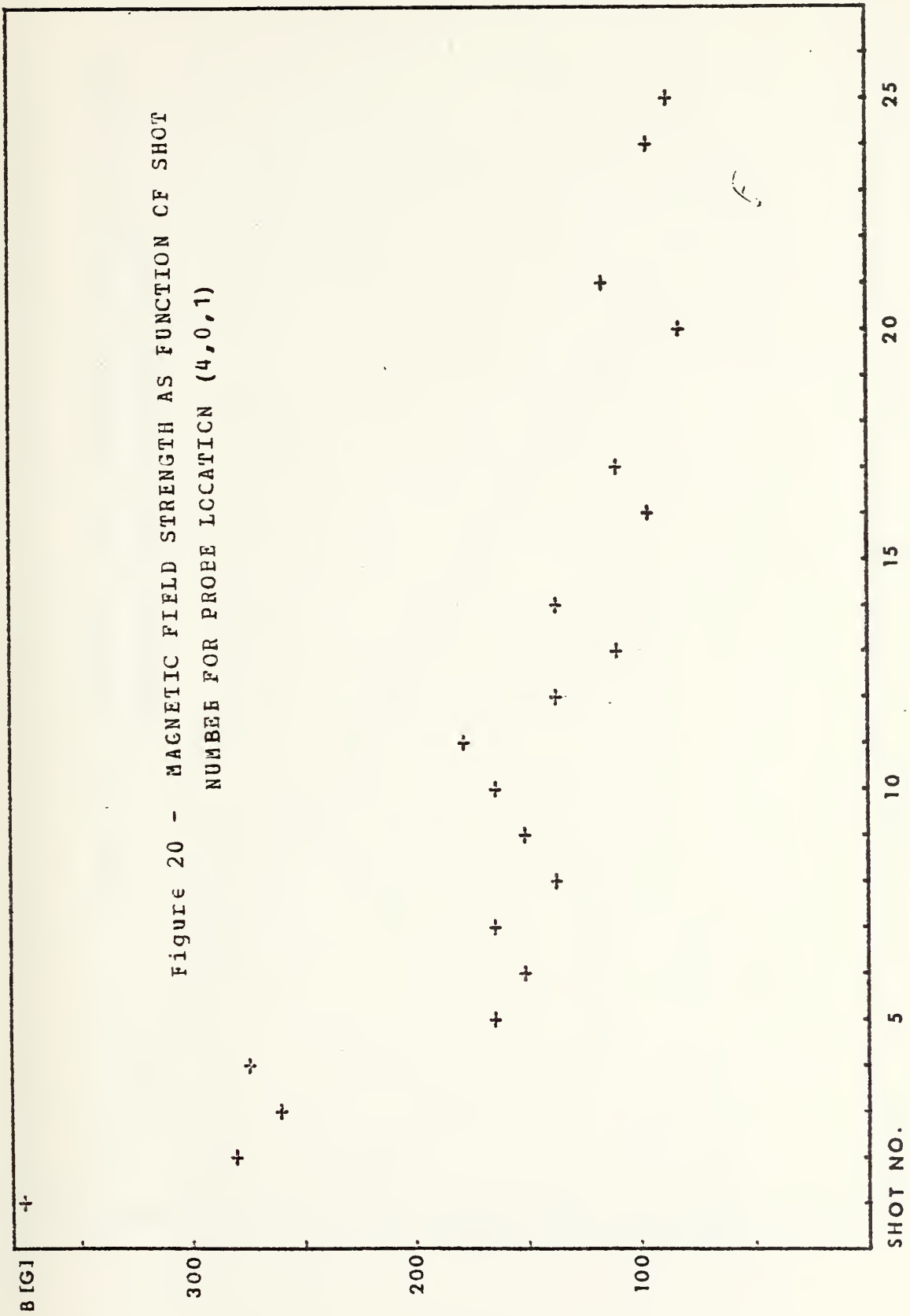


Figure 17 - MEASURED ELECTRON TEMPERATURE AS FUNCTION OF IRRADIANCE

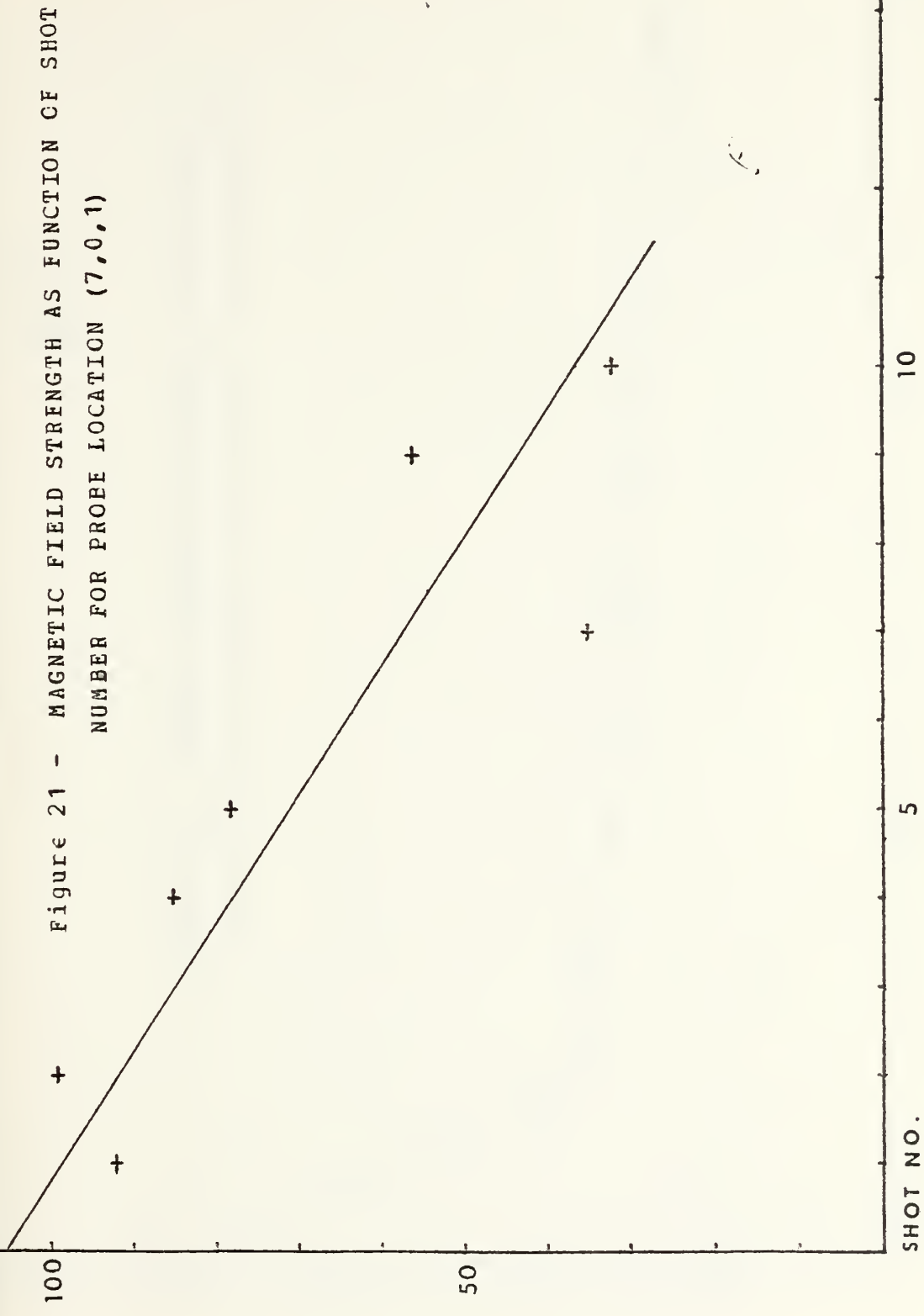






BIGI

Figure 21 - MAGNETIC FIELD STRENGTH AS FUNCTION OF SHOT
NUMBER FOR PROBE LOCATION (7,0,1)



B* [G/J]

(3,0,1.5)
AIR

Figure 22 - ENERGY NORMALIZED MAGNETIC FIELD [G/J] AS
FUNCTION OF SHCT NUMBER- BEST LINEAR FIT SUPERIMPOSED

150

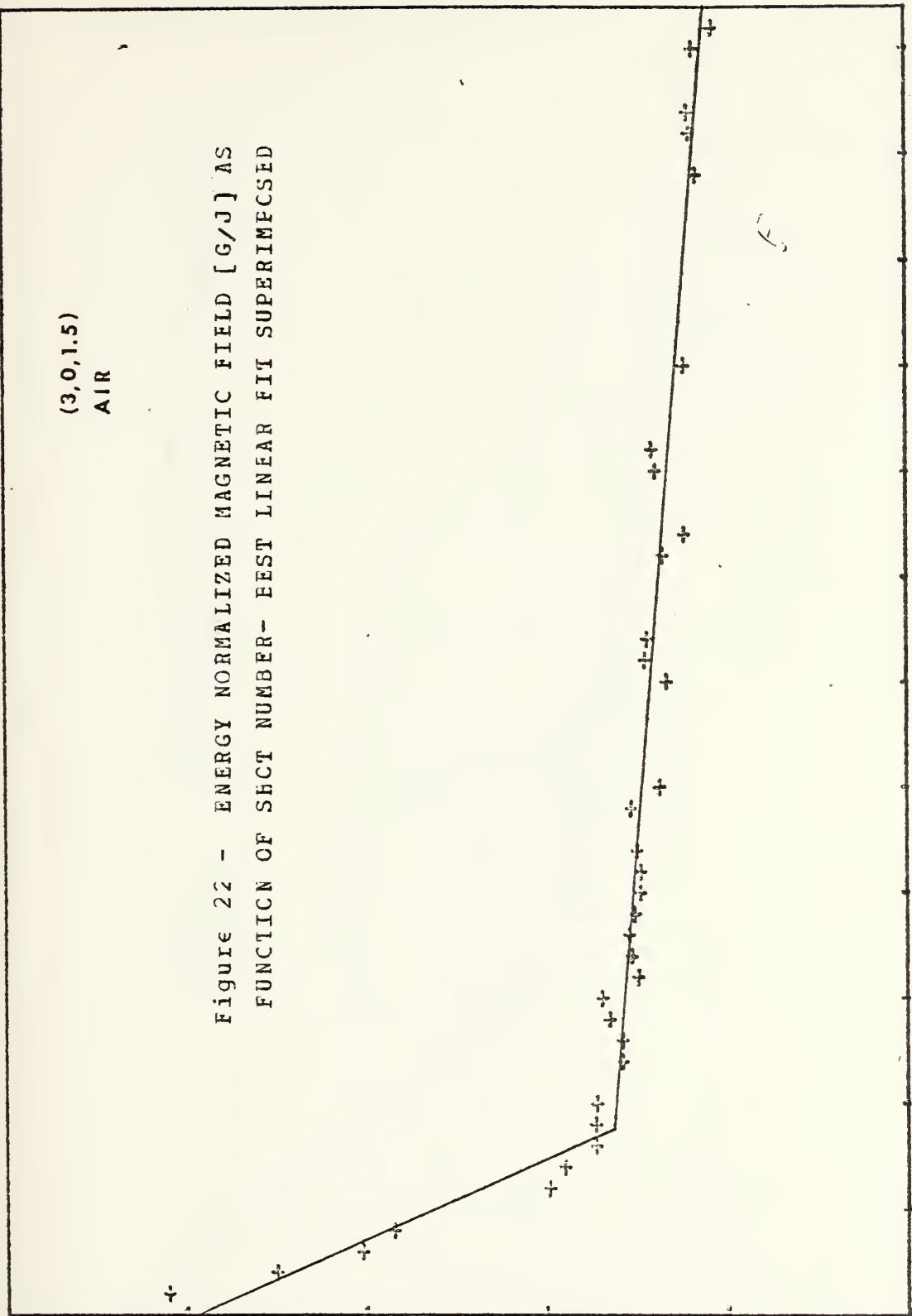
50

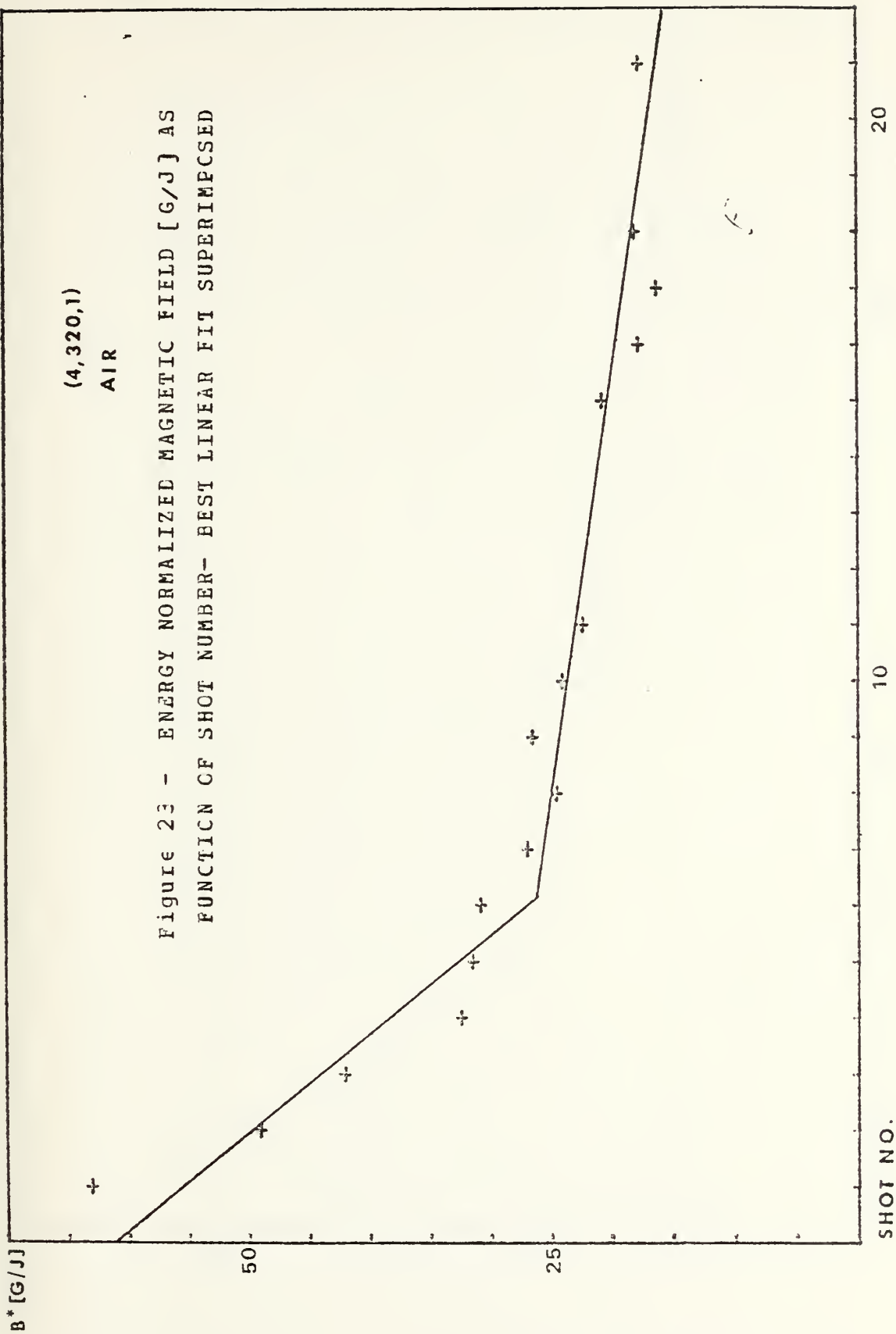
60

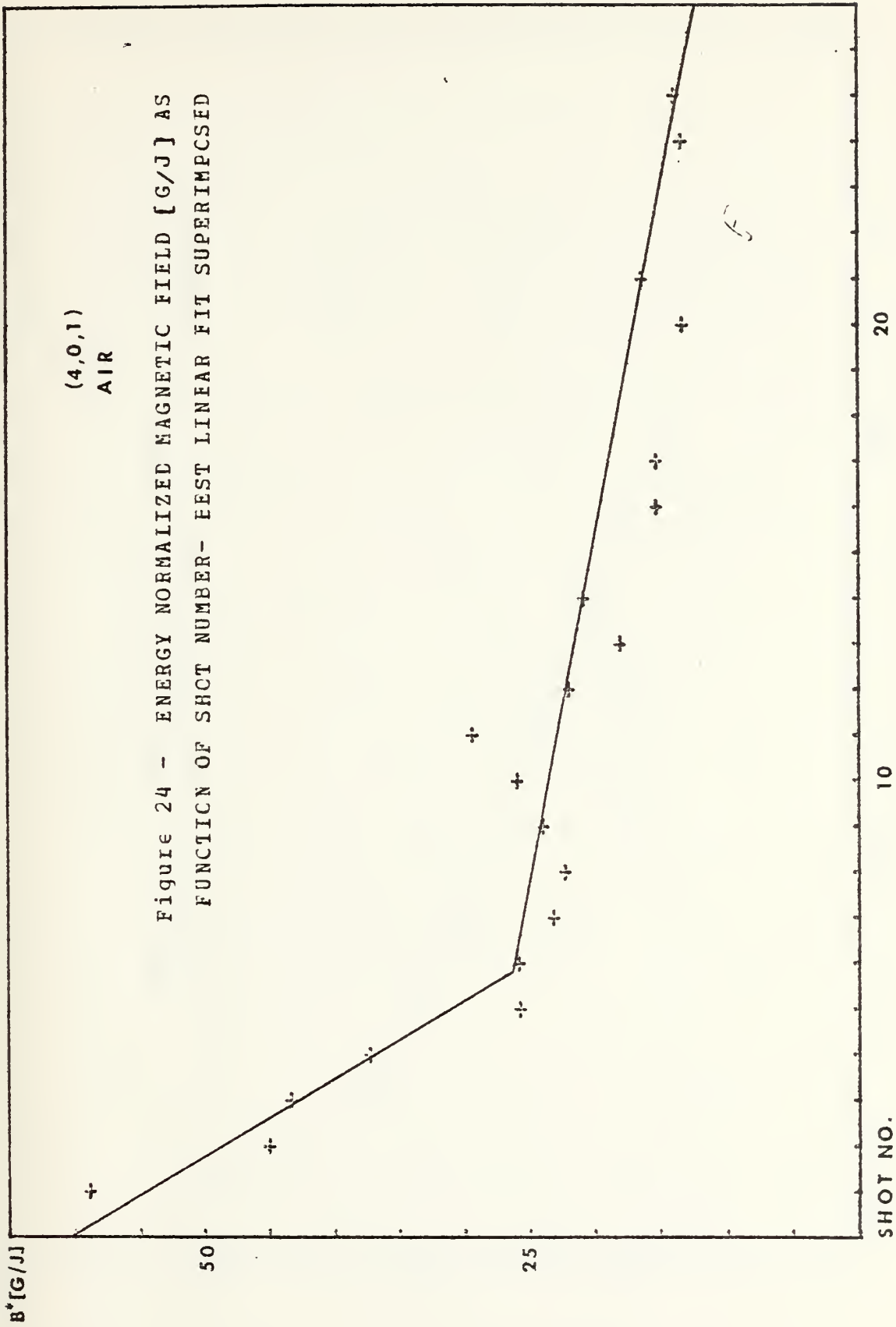
40

20

SHOT NO.

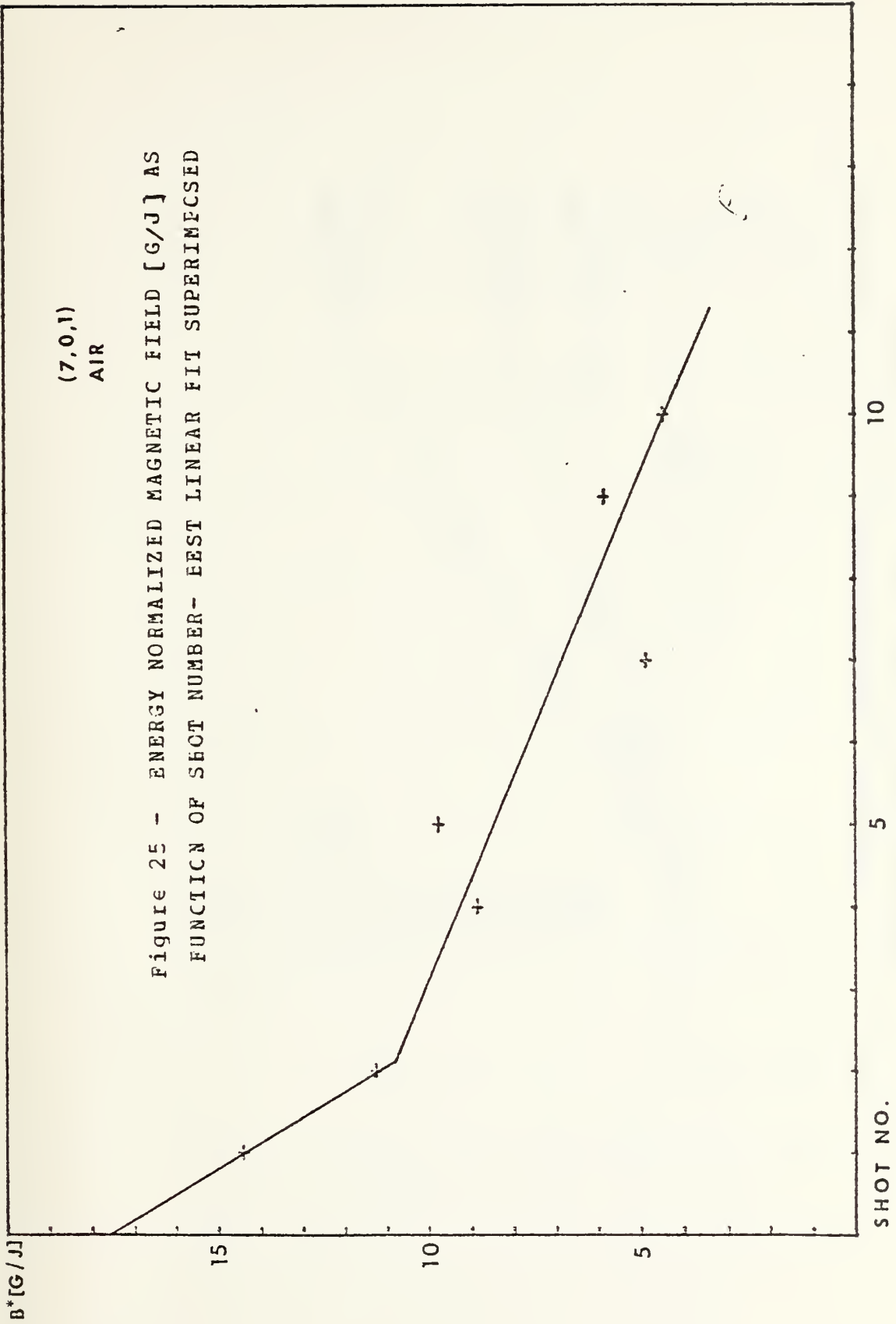






(7,0,1)
AIR

Figure 25 - ENERGY NORMALIZED MAGNETIC FIELD [G/J] AS
FUNCTION OF SHOT NUMBER- BEST LINEAR FIT SUPERIMPOSED



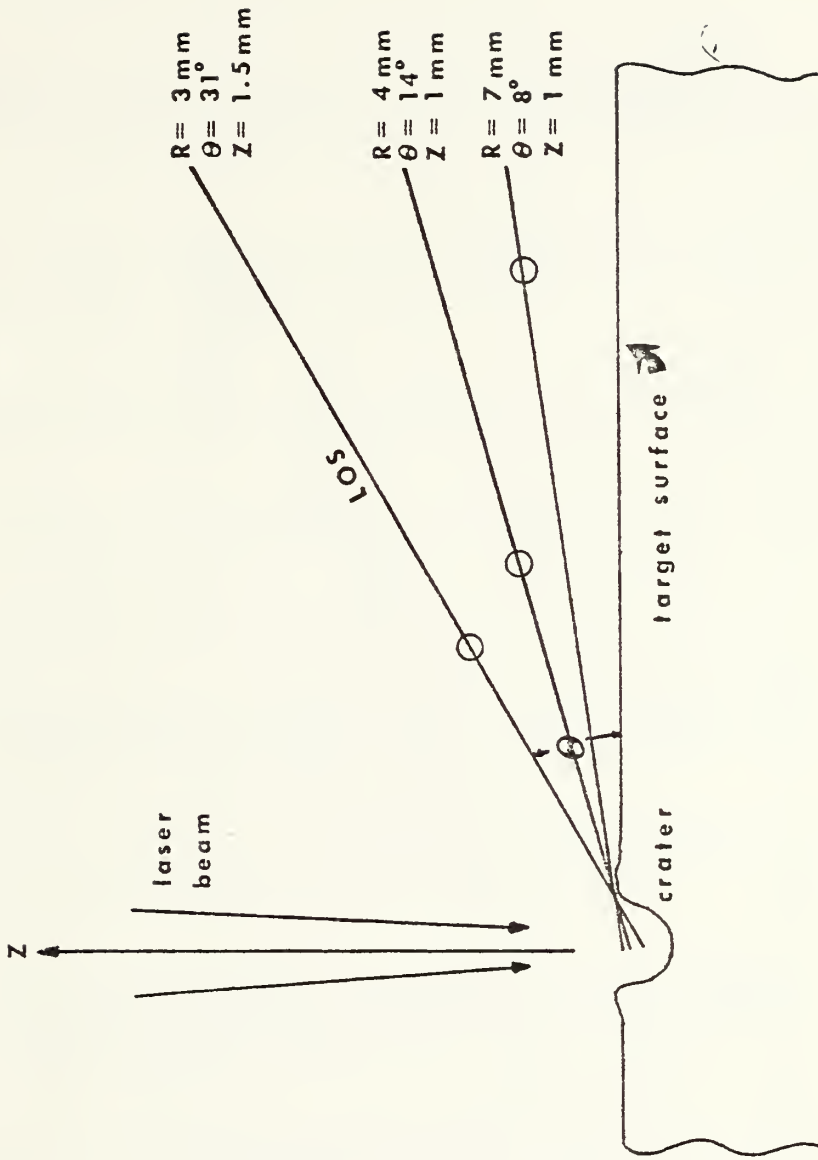


Figure 26 - GRAPHICAL REPRESENTATION OF LINE OF SIGHT FROM ERCBE POSITIONS TO THE CENTER OF THE CRATER

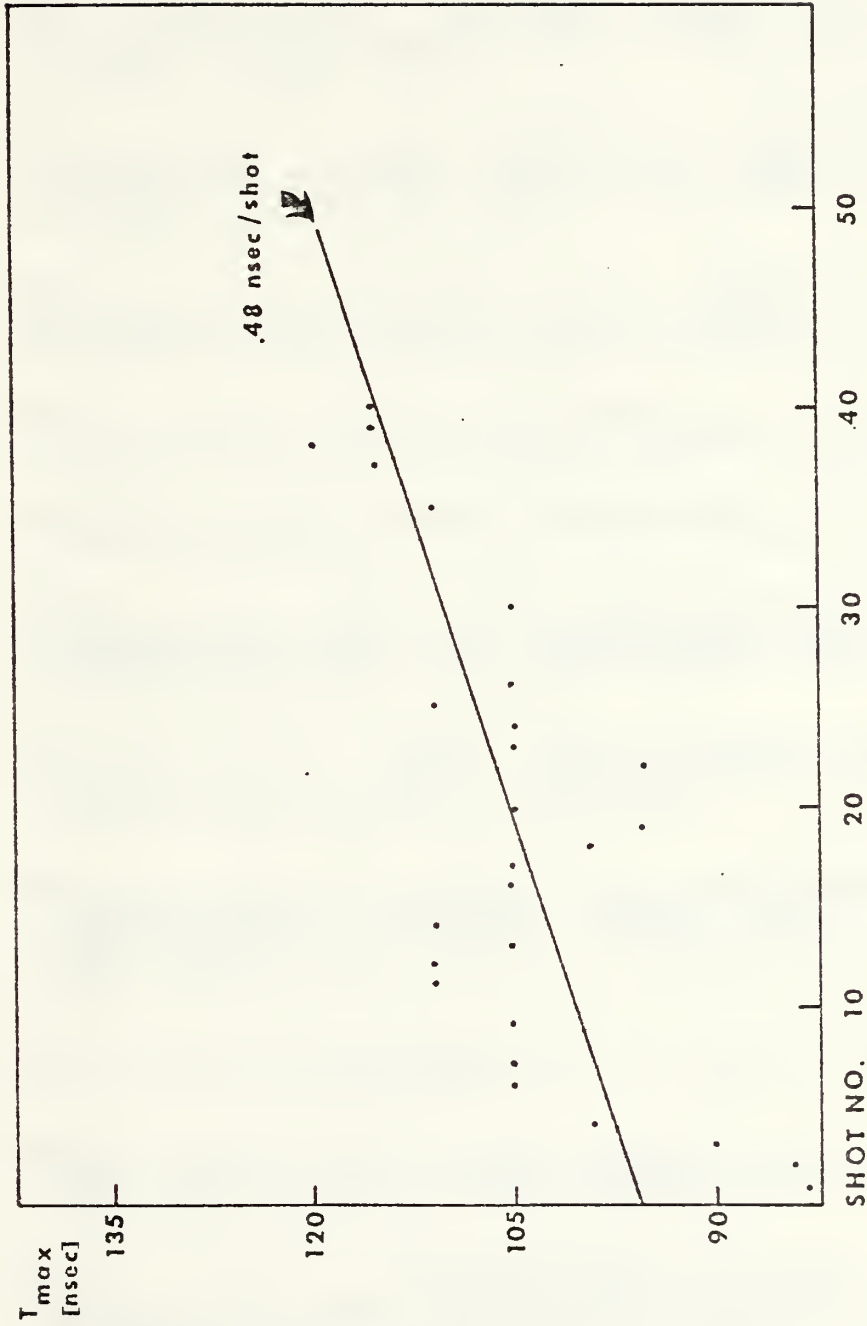


Figure 27 - ARRIVAL TIME OF PEAK OF MAGNETIC FIELD SIGNAL
AS FUNCTION OF SHOT NUMBER

LIST OF REFERENCES

1. Basov ,N.G., and others, "High Temperature Effects of Intense Laser Emission Focused on a Solid Target," Soviet Physics JETP, v. 27, no. 4, pp. 575-582, October 1966.
2. Bird , R.S., The Pressure Dependence of Spontaneous Magnetic Fields in Laser Produced Plasma, Ph.D. Thesis, Naval Postgraduate School, Monterey, California, 1973.
3. Bleach , R. D. and Nagel, D. J., Craters Produced by High Power-Density Lasers, paper presented at ASME Convention, Houston, Texas, November 30 1975.
4. Bogen P., Plasma diagnostics, (edited by W. Lochte-Holtgreven), p. 424-477, Wiley, 1968.
5. Botticher , W., Plasma Diagnostics (edited by W. Lochte-Holtgreven) , p. 617-643 , Wiley, 1968.
6. Brooks ,K M, Sr., An Investigation of Early Disturbances Found in Association with Laser Produced Plasmas, MS Thesis, Naval Postgraduate School, Monterey, California, 1973.
7. Callahan , D. J., Laser Plasma Particle Velocities , MS Thesis , Naval Postgraduate School , Monterey, California , June 1976.
8. Case , R. S., Jr., An Investigation F Self-Generated Magnetic Fields and Electron Emission in Laser Produced Plasmas, Ph.D. Thesis, Naval Postgraduate School, Monterey, California, March 1974.
9. Chen , F. F., Introduction to Plasma Physics, p. 322, Plenum Press, 1974.
10. Dawson , J. M., "On the Production of Plasma by Giant Pulse Laser," Phy. Fluids, v. 7, no. 7, p. 981, 1964.
11. Davis , L. J., Self-Generated Magnetic Fields Produced by Laser Bombardment of a Solid Target, MS Thesis, Naval Postgraduate School, Monterey, California, 1971.

12. Dean S.O., and others, "Demonstration of Collisionless Interactions Between Interstreaming Ions in a Laser-Produced-Plasma Experiment," Physical Review Letters, v. 27, no. 8, p. 487-490, 23 August 1971.
13. Drouet M.G., and Bolton, R., Distribution of Self-Generated Current in Laser-Produced Plasmas, Direction Sciences de base, Institut de recherche de L'Hydro-Quebec, Varennes, Quebec, 3 November 1975.
14. Ginzburg, V.L., Electromagnetic Waves in Plasmas [Pergamon, New York, 1970] Sect. 20, J.P. Friedberg, R.W. Mitchell, R.L. Morse, and L.I. Rudsinski, Physical Review Letters, v. 28, 795, 1972.
15. Griem H.R., Plasma Spectroscopy, p. 580, McGraw-Hill, 1964.
16. Jahoda, F.C., and others, "Continuum Radiation in the X-ray and Visible Regions from a Magnetically Compressed Plasma (Scylla)," Physical Review, v. 119, p.843-856, 1 August 1960.
17. Koopman, D.W., "Momentum Transfer Interaction of a Laser Produced Plasma with a Low-Pressure Background," Phys. Fluids, v. 15, no. 11, p. 1959-1969, November 1972.
18. Korobkin, V.V. and Serov, R.V., "Investigation of the Magnetic Field of a Spark Produced by Focussing Laser Radiation," JETP Letters, v. 4., no. 3, p.102-106, 1 August 1966.
19. McKee L.L., An Investigation of the Self-Generated Magnetic Associated with a Laser Produced Plasma, Ph.D. Thesis, Naval Postgraduate School, Monterey, California, 1972.
20. McLaughlin, F. A., Inductive Magnetic Probe Diagnostics in a Plasma, MS Thesis, Naval Postgraduate School, Monterey, California, 1970.
21. Mulser, P and others, "Plasma Production by Laser" Physics Reports, v. 6c, p.189-239, January 1973.
22. Naval Research Laboratory Report 6541, Calculations Useful in the Determination of Electron Temperature from X-ray Continuum Radiation Emitted from High Temperature Plasmas, by R.C. Elton and A. D. Anderson, p.36, 31 March 1967.
23. Naval Research Laboratory Report 6738, Determination of Electron Temperatures Between 10eV and 100keV from X-ray Continuum Radiation in Plasmas, by R.C. Elton, v.42, p. 1823-1824, December 1971.

24. Naval Research Laboratory Report 7411, Laser-Induced Sources for Magnetic Fields, by J.A. Stamper, p. 7-10, 16 June 1972.
25. Phillips, R. C. and Turner, E. B., "Construction and Calibration Techniques of High Frequency Magnetic Probes," The Review of Scientific Instruments, v. 36-12, p. 1822-1825, December 1965.
26. Podgorni, I.M., Topics in Plasma Diagnostics, p. 113-124, Plenum Press, 1971.
27. Ready, J. F., Effects of High-Power Laser Radiation, Academic Press, 1971.
28. Richtmyer, F. K., Kennard, E. H. and Copper, J. N., Introduction to Modern Physics, 6th ed., McGraw-Hill, 1959.
29. Rose, D.J. and Clark M., Plasma and Controlled Fusion, p. 228-236, MIT Press and Wiley, 1951.
30. Schwirzke, F., Measurements of Spontaneous Magnetic Fields in Laser Produced Plasmas, paper presented at the Third Workshop on "Laser Interaction and Related Plasma Phenomena," Rensselaer Polytechnic Institute, Troy, New York, August 13-17, 1973.
31. Shewchuk, S.A., X-Ray Diagnostics of Laser-Produced Aluminum Plasmas, MS Thesis, Naval Postgraduate School, Monterey, California, 1976.
32. Spitzer, L., Jr., Physics of Fully Ionized Gases, 2d ed., p. 138, Wiley, 1962.
33. Stamper, J. A. and others, "Spontaneous Magnetic Fields in Laser Produced Plasmas," Physical Review Letters, v. 26, no. 17, p. 1072-1015, 26 April 1971.
34. Stamper, J. A. and Tidman, D. A., "Magnetic Field Generation due to Radiation Pressure in a Laser-produced Plasma," Phys. Fluids, v. 16, no. 11, p. 2024-2025, November 1973.
35. Wegener, B., Measurements of Early Magnetic Fields in Laser Produced Plasma, MS Thesis, Naval Postgraduate School, Monterey, California, June 1974.
36. Whitney, K. G. and Davis, J., "Conversion Efficiencies of Laser to X-Ray Energy in C, F, and Al Plasmas," Applied Physics Letters, v. 24, no. 10, 15 May 1974.

37. Winsor, N. K. and Tidman, D. A., "Laser Target Model," Physical Review Letters, v. 31, no. 17, p. 1044, 22 October 1973.
38. Wright, T.P., "Comments on 'Demonstration of Collisionless Interactions Between Interstreaming Ions in a Laser-Produced-Plasma Experiment'," Physical Review Letters, v. 28, no. 5, p. 268-270, 31 January 1972.

INITIAL DISTRIBUTION LIST

	No. Copies
1. Defense Documentation Center Cameron Station Alexandria, Virginia 22314	2
2. Library , Code 0212 Naval Postgraduate School Monterey, California 93940	2
3. Department Chairman, Code 61 Wh Department of Physics and Chemistry Naval Postgraduate School Monterey, California 93940	2
4. Professor F. Schwirzke, Code 61 Sw Department of Physics and Chemistry Naval Postgraduate School Monterey, California 93940	2
5. Professor A. W. Cooper, Code 61 Cr Department of Physics and Chemistry Naval Postgraduate School Monterey, California 93940	2
6. Lieutenant Commander F. T. Williamson Armed Forces Staff College 7800 Hampton Blvd Norfolk, Virginia 23511	1

thesW6243

Laser generated magnetic fields.



3 2768 001 90104 4

DUDLEY KNOX LIBRARY